ScienceAdvances AAAS

Manuscript Template

FRONT MATTER

Title

- Identification of different oxygen species in oxide nanostructures with ^{17}O solid-state NMR spectroscopy
- Identifying oxygen ions in nano-oxides

Authors

Meng Wang[1], Xin-Ping Wu[2], Sujuan Zheng[1], Li Zhao[1], Lei Li[1], Li Shen[1], Yuxian Gao[3], Nianhua Xue[1], Xuefeng Guo[1], Weixin Huang[3], Zhehong Gan[4], Frédéric Blanc[5,6], Zhiwu Yu[7], Xiaokang Ke[1], Weiping Ding[1], Xue-Qing Gong[2]*, Clare P. Grey[5,8]* and Luming Peng[1]*

Affiliations

[1] Key Laboratory of Mesoscopic Chemistry of Ministry of Education, School of Chemistry and Chemical Engineering, Nanjing University, Nanjing 210093, China.

[2] Key Laboratory for Advanced Materials, Centre for Computational Chemistry and Research Institute of Industrial Catalysis, East China University of Science and Technology, 130 Meilong Road, Shanghai 200237, China.

[3] Department of Chemical Physics, University of Science and Technology of China, Hefei 230026, China.

[4] National High Magnetic Field Laboratory, 1800 E. Paul Dirac Drive, Tallahassee, FL, 32310–3706, USA.

[5] Department of Chemistry, University of Cambridge, Lensfield Road, Cambridge, CB2 1EW, UK.

[6] Department of Chemistry and Stephenson Institute for Renewable Energy, University of Liverpool, Crown Street, L69 7ZD, UK.

[7] High Magnetic Field Laboratory, Chinese Academy of Sciences, Hefei 230031, China.

[8] Department of Chemistry, Stony Brook University, Stony Brook, NY 11974-3400, USA.

Corresponding author. Emails: luming@nju.edu.cn (L.P.); xgong@ecust.edu.cn (X.-Q.G.) and cpg27@cam.ac.uk (C.P.G.)

Abstract

Nanostructured oxides find multiple uses in a diverse range of applications including catalysis, energy storage and environmental management, their higher surface areas and, in some cases, electronic properties, resulting in different physical properties from their bulk counterparts. Developing structure-property relations for these materials requires a determination of surface and subsurface structure. Although microscopy plays a critical role, owing to the fact that the volumes sampled by such techniques may not be representative of the whole sample, complementary characterization methods are urgently required. Here we develop a simple NMR strategy to detect the first few layers of a nanomaterial, demonstrating the approach with technologically relevant ceria nanoparticles. We show that the ^{17}O resonances arising from the 1st to 3rd surface layer oxygen ions, hydroxyl sites and oxygen species near vacancies can be distinguished from the oxygen ions in the bulk, higher frequency ^{17}O chemical shifts being observed for the lower coordinated surface sites. $H_2{}^{17}O$ can be used to selectively enrich surface sites, allowing these and only these particular active sites monitored in a chemical process. ^{17}O NMR spectra of thermally treated nanosized ceria clearly show how different oxygen species

interconvert at elevated temperature. DFT calculations confirm the assignments and reveal a strong dependence of chemical shift on the nature of the surface. The results presented here opens up new strategies for characterizing nanostructured oxides and their applications.

MAIN TEXT

Introduction

As the only nuclear magnetic resonance (NMR) active oxygen stable isotope, ^{17}O NMR spectra have been collected for a large range of metal oxides[1-3] and reveal that ^{17}O is extremely sensitive to the local environment of the oxygen resulting in a very large chemical shift range larger than 1,000 ppm[4]. However, only a few reports have been published on nanosized oxides[5, 6], despite their use in numerous applications[7, 8]. This is largely a result of the high cost of ^{17}O enrichment, generally necessary due to the low natural abundance of ^{17}O (0.037%), and the difficulties associated with efficient isotopic enrichment of the nanomaterials, (for example, heat treatment in ^{17}O enriched O_2 gas, a common method for ^{17}O enrichment, generally leads to particle sintering). However, the low natural abundance of the bulk also brings new possibilities for selective labelling and detection of specific sites.

NMR spectroscopy, which is sensitive to the short-range order of all the resonant nuclei in the sample investigated, should be ideal to study nanomaterials, where the long-range order is usually interrupted by the surface and other defect sites. At the same time, as one of the most extensively studied nano-oxides, ceria nanostructures, have been studied for use in a wide range of applications from solid oxide fuel cell[9] and catalysis[10] (in, for example, catalytic convertors[11]) to biological applications[12]. Therefore, we demonstrate our novel ^{17}O NMR

approach with this nanomaterial. In addition to the finding that different oxygen species (oxygen ions in different layers and different surfaces), can be distinguished in ^{17}O NMR, we discover that hydroxyl groups can form through water dissociation on ceria nanoparticles and this process can be exploited to produce an efficient and selective ^{17}O labelling method for the surface of nanosized oxides.

Results

Ceria nanoparticles were prepared hydrothermally[13] and their structures were confirmed by X-ray diffraction (XRD; Fig. S1A). Broader peak were observed in the XRD patterns consistent with the small particle sizes (~3 nm), as indicated by the TEM images (Fig. S1B). Although the ceria nanoparticles exhibit mostly rounded shaped or polyhedral morphologies, according to previous experimental observations [14] as well as theoretical calculations [15], the surfaces are dominated by the thermodynamically most stable (111) face (Fig. S1B).

^{17}O enrichment was conducted by heating the ~3 nm nanoparticles in a $^{17}O_2$ gas atmosphere at different temperatures. The mean diameters, calculated based on the XRD data by using the Debye-Scherrer equation, increase with increasing enrichment temperature (Fig. S2 and Table S1) from approximately 4 to 42 nm following calcination at 523 and 1073 K, respectively. The results are consistent with BET surface area data (Table S2), which show a drop in surface area from 190 to 6 $m^2 \cdot g^{-1}$ over the same temperature range.

The ^{17}O magic angle spinning (MAS) NMR spectra of the ceria nanoparticles are compared with the "bulk" ceria, i.e., micron-sized $Ce^{17}O_2$ particles (commercial reagent CeO_2 obtained from Sinopharm Chemical Reagent Co., Ltd. enriched in $^{17}O_2$ gas, also see Fig. S1 and S3), in

Fig. 1A. Bulk ceria contains one sharp resonance at 877 ppm corresponding to the 4-coordinated oxygen ion (OCe_4) site, consistent with previous studies.[16] The resonances are much broader for the nanoparticles and three additional peaks at approximately 1040, 920 and 825 ppm are observed. The positions of these resonances do not change in spectra acquired with different external magnetic fields (14.1 vs. 9.4 T), indicating that these peaks arise from species with small quadrupolar coupling constants (C_Qs). The intensities of the three new peaks decrease (relative to the resonance at 877 ppm) with increasing particle sizes, suggesting that these species are related to surface and sub-surface sites or other defect sites (e.g., sites nearby oxygen vacancies)[17]. The width of these peaks must reflect the large distribution of chemical shifts for the different surface and sub-surface environments, as well as relatively wide size distribution of the nanosized sample (Fig. S1). The longitudinal relaxation times (T_1) associated with the new peaks are shorter than that of the bulk environment again implying these sites may be nearby defects (Fig. S4).

First-principles density function theory (DFT) calculations were performed to aid the spectral assignments. The CeO_2(111) surface was considered initially (on the basis of the TEM results), and a slab model composed of 6 layers of cerium and 12 layers of oxygen ions (6 CeO_2 tri-layers) was constructed for the calculations (Fig. 1B), where the oxygen ions at the same layer have the same local bonding environments and thus have the same chemical shift (δ_{iso}), C_Q and asymmetry parameter (η_Q) within each layer. The oxygen ions in the centre layers (4^{th} to 9^{th} layer) have similar calculated chemical shifts of ~880 ppm (Fig. 1B), which are close to the experimental chemical shift of oxygen ions in bulk ceria (877 ppm, Fig. 1A)[16]. For the top and bottom 3 layers, however, very different chemical shifts at approximately 1033, 921 and 837 ppm (with small C_Q values smaller than 0.14 MHz, Table S3), were calculated for oxygen ions at the 1^{st} , 2^{nd} and 3^{rd} layer of the slab, respectively. These chemical shift values are surprisingly

close to those of the three additional peaks observed in NMR spectra of the ceria nanoparticles. On this basis, the peaks at 1040, 920 and 825 ppm (Fig. 1A) can be tentatively assigned to the oxygen ions at the outmost 1st, 2nd and 3rd layers of the particles, respectively. Previously, the dependence of chemical shift on the atomic position with respect to the surface was predicted and observed experimentally only in ^{77}Se NMR of ZnSe nanoparticles, however, the peaks owing to different layers were not clearly resolved[(18)]. The assignment of the peak at 1040 ppm to the 1st layer (3-coordinated) oxygen (on the (111) surface) is in agreement with the trend that the oxygen chemical shift moves to higher frequency as the coordination number decreases in simple metal oxides[(3)]. The fractions of 1st layer oxygen ions (extracted by using spectral deconvolution) is in accordance with the predictions from BET measurements (Fig. S5). The quadrupolar coupling constants of these oxygen ions predicted from DFT calculations are also small (Table S3, ν_Q smaller than the radio frequency field amplitude ν_1 of 62.5 kHz).

Calculations were also performed for other low index surfaces, such as the (110) and (100) surfaces (Fig. S6), which may also be present in the nanoparticles. In all the surfaces explored, the oxygen ions on the first layer have lower coordination numbers and give rise to shifts at higher frequencies (>1,000 ppm), which is again in agreement with the trend that the oxygen chemical shift appears at a higher frequency with less coordination numbers in simple metal oxides[(3)]. The shift calculated for the (110) surface sites is 1061 ppm, somewhat similar to the value for (111) surface. Very different shifts of around 1129 ppm were, however, calculated for the (100) surface sites, the higher frequency shift arising from the lower O coordination numbers (2-coordinated sites, as compared to 3-coordinated sites for the (111) and (110) surfaces). The lack of a resonance in this chemical shift range in our experimental spectra (Fig. 1A) is in agreement with reports that this is the least energetically favourable low-index surface[(15)]. The large difference between the calculated chemical shifts for oxygen ions on the (111) and (100)

surfaces (i.e., 1129 and 1033 ppm), as well as our experimental observations that match well with calculations of (111) facets, suggest that the ^{17}O NMR shift may be able to probe the coordination numbers of the oxygen atoms and the exposed surface planes of nanocrystals, which can be extremely important for their applications[(19)].

To provide additional support for the spectral assignments and to explore the surface structure and chemistry of ceria nanoparticles, natural abundance water was adsorbed on the ^{17}O-enriched ceria samples. The major ^{17}O resonance at 877 ppm from to OCe_4 (bulk ceria) remains in the NMR spectra of these samples (Fig. 2A) since the oxygen ions in the bulk are not expected to be affected by surface adsorbates. The resonances at around 1040, 920 and 825 ppm, however, disappear and a new broad shoulder at approximately 850 ppm can be observed. The shift of this resonance remains unchanged in the spectrum acquired at an ultrahigh field of 19.4 T, indicating the resonance is associated with a small C_Q (Fig. S7, Fig. S8A and Table S4). In addition, another broad peak is observed at much lower frequency (32 ppm). This peak disappears after the sample is dried under vacuum at room temperature, suggesting that this resonance can be assigned to water adsorbed on the surface of ceria. After thermal treatment of the sample at 573 K, the broad peak at 850 ppm disappears and the peaks at 1040, 920 and 825 ppm can be observed again, the spectrum resembles that of the original bare ceria nanoparticles; this indicates that the structure of the ceria nanoparticles is recovered at elevated temperature when water is completely removed. The resonance at 850 ppm is ascribed to the oxygen ions in the 3rd layer (these environments resonating at 825 ppm in the dry sample), in agreement with DFT calculations (Fig. S8 and Table S5). The resonances from the oxygen ions on the 1st and 2nd layer are not observed when water is adsorbed, presumably because of fast exchange between these oxygen ions with water; this hypothesis will be further explored below.

Interactions between ceria nanoparticles and water were also investigated in a reverse way, via the adsorption of ^{17}O enriched water on non-enriched ceria nanoparticles (preheated at 573 K). On adding $H_2{}^{17}O$ dropwise to ceria nanoparticles at room temperature, weak peaks at approximately 1040, 877 and 270 ppm appeared (Fig. 2B) in addition to the broad peak at around 32 ppm from adsorbed water. These peaks dominated the spectra after the sample was dried under vacuum at 373 K. Similar spectra were obtained by introducing $H_2{}^{17}O$ to non-enriched ceria nanoparticles calcined at 573 K on a vacuum line (Fig. 2B). The broad resonance at 270 ppm can be tentatively assigned to the hydroxyl groups (Ce^{4+}-^{17}OH) observed previously by FT-IR[(20)] on the surface of ceria nanoparticles on the basis of the low chemical shift. ^{17}O-^{1}H double resonance NMR techniques (in this case, Cross Polarization (CP)[(21)] and Rotational Echo Double Resonance (REDOR)[(22)]) were used to confirm this assignment since they can be used to select the ^{17}O resonances of oxygen ions close to protons: they measure the heteronuclear dipolar coupling (i.e., between ^{17}O and ^{1}H), a function of distance between ^{17}O and ^{1}H. As seen from Fig. 3A, both the REDOR difference spectrum and CP spectra only show one signal at 270 ppm, confirming that this resonance comes from oxygen ions in close proximity to proton. The NMR parameters of this species, including chemical shift (δ_{iso}) and quadrupolar product ($P_Q = C_Q(1+\eta_Q^2/3)^{1/2}$), were extracted by calculating the frequency change of the centre of gravity of the signal at different external fields (300 ppm at 14.1 T vs. 270 ppm at 9.4 T). The obtained values (δ_{iso} = 325 ppm, P_Q = 5.1 MHz) are also supported by the DFT calculation results (Fig. S8 and Table S5). It is clear that the surface hydroxyl groups are associated with much larger C_Q than the less coordinated surface oxygen species and this is in agreement with the nutation curve (Fig. S9). The CP build-up curve (Fig. 3B) shows that with a short contact time (<100 μs), the CP intensity increases rapidly and reaches a maximum at around 90-100 μs. With longer contact times, the signal decreases significantly. This CP behaviour resembles the oxygen ions at

Brønsted acid sites in acidic zeolites[23], as well as hydroxyl oxygen species in layered double hydroxides[24], indicating that this O species is directly bound to H. ^{1}H-^{17}O TRAPDOR NMR was also used to investigate the ^{1}H-^{17}O dipolar coupling on the surface of ceria nanoparticles (Fig. S10). Significant TRAPDOR fraction can be observed at a rather short ^{17}O irradiation time of about 100 μs and this value reaches maximum at around 140 μs, very similar to the observation in acidic zeolite HY[23], and again this result suggests that H is directly connected to O. Furthermore, the maximum TRAPDOR effect of ~23 % shows the ^{17}O isotopic molar percentage among the surface hydroxyl groups, indicating highly efficient ^{17}O isotopic labelling of the surface of ceria nanoparticles.

The domination of the surface species (i.e., the lower coordinated oxygen ions at ~1040 and hydroxyl groups at ~270 ppm) in the spectra of natural abundance ceria nanoparticles adsorbed with ^{17}O water, indicates that we can use this approach to as an efficient and surface-selective isotopic enrichment method. To demonstrate this, we use this method to confirm our proposal that the resonances at 1040 and 920 ppm are owing to surface and subsurface oxygen sites, specifically those on the (111) surface. To achieve this, we selectively enriched the surfaces of ceria nanorods with $H_2{}^{17}O$ at room temperature, since these are dominated by distinct (111) facets (Fig. S11A). Ceria nanorods were also non-selectively enriched in a $^{17}O_2$ atmosphere at 923 K for comparison. Four sharp resonances at 1027, 920, 877 and 825 ppm are seen for the sample enriched in $^{17}O_2$, while the peak at 877 ppm owing to bulk oxygen species dominates (Fig. S11B). For nanorods enriched with $H_2{}^{17}O$, however, the majority of the signal comes from two sharp resonances 1027 and 920 ppm (Fig. S11C), confirming our assignment of these resonances to the (111) surface and subsurface sites, respectively. A broad peak with maximum intensity at 270 ppm arising from OH can also be observed in the surface labelled sample. The broadening seen in the nanoparticles presumably occurs because a larger range of surfaces and

disorder is present. This approach shows that selectively labelling[25], which should be based on water adsorbing/dissociation, can be now controlled to the first a few layers of surface sites for oxide nanostructures.

The fact that significant surface ^{17}O species were observed only on ceria nanoparticles but not on bulk ceria by adsorbing $H_2{}^{17}O$ (Fig. 2B), implies that water dissociation readily occurs only at the surface of the more active ceria nanoparticles. Calculations show that the oxygen vacancy formation energies at the outmost 1st and 2nd layers are substantially smaller than that of the 3rd to 6th layers (Fig. S12), suggesting that there are more oxygen vacancies on the 1st and 2nd layers of ceria. Therefore, water dissociation on ceria nanoparticles is more likely to be the results of water interacting with oxygen vacancies. These observations also agree with the presence of the adsorbed water peak at ~ 32 ppm when adsorbing non-enriched water on ^{17}O enriched nanosized ceria. Adsorption of water on nanosized ceria proves effective for ceria nanoparticles with a diameter as large as 16 nm (Fig. S13). The relative intensity of the peak at around 270 ppm assigned to the hydroxyl groups decreases with increasing pre-heating temperature, compared to the peaks at approximately 1040 and 920 ppm arising from 1st and 2nd layer surface oxygen ions, suggesting that the concentration of oxygen vacancies on the surface of the ceria nanoparticles decreases with increasing particle size.

With all the signals being assigned, the evolution of different species on the ceria nanoparticles during thermal treatment was then examined (Fig. 4). At 373 K, the intensities of the peaks from the surface oxygen species (1040 and 270 ppm) are much stronger than peak arising from the oxygen ion in bulk ceria (877 ppm). With increasing temperature, the peaks arising from surface become weaker while the intensity of the peak for bulk oxygen species increases. The latter becomes the major resonance at the temperature above 573 K, indicating that at temperatures higher than 423 K, oxygen ions on the surface can efficiently exchange with

oxygen ions in the bulk, presumably through oxygen migration via oxygen vacancies. Nanoparticle sintering can be excluded as a source of the oxygen exchange process, at least at a temperature lower than 573 K, since all of the samples were preheated at 573 K. Therefore, this approach can be used to track the motion of oxygen ions in oxide nanostructures as a function of temperature.

Oxygen vacancies and Ce^{3+} are often present as defects in CeO_2-based materials, and their concentrations are significant in nanoparticles[17, 26], which can be determined by X-ray photoelectron spectroscopy (XPS)[27, 28] (Fig. S14 and S15). These species play an important role in controlling the physical properties of this material for a variety of applications, such as heterogeneous catalysis of redox reactions[29] and are thus investigated here with NMR. H_2 temperature programmed reduction (TPR) experiments were first carried out on bulk ceria and ceria nanoparticles to determine the temperature to generate Ce^{3+} and oxygen vacancy in H_2 atmosphere (Fig. S16). For bulk ceria, a small and relatively narrow H_2 consumption peak can be observed at a temperature lower than 800 K, while a much broader and more intense peak centred at 773 K is seen for ceria nanoparticles calcined at 773 K. These peaks can be ascribed to reaction of H_2 with surface oxygen of ceria[30]. Again, the large peak width associated with the nanoparticles can be ascribed to the wide size distribution of the nanosized sample (Fig. S1). The consumption of H_2 increase again at a temperature above 1050 K, which should be associated with the bulk oxygen species. Thus, the ^{17}O NMR spectrum were collected for bulk ceria enriched at 1073 K and then reduced in H_2 atmosphere at 1073 K (Fig. 5A). A shoulder to lower frequency of the OCe_4 peak (877 ppm) and a more distinct lower frequency resonance at around 845 ppm with a full width at half maximum of 12 ppm can be observed. The lower frequency components are tentatively assigned to oxygen ions nearby the oxygen vacancies or in the Ce^{3+} second cation coordination shell. The spectrum of ceria nanoparticles initially enriched at 773 K

and then reduced at 773 K in H_2 also contains a relatively broad resonance with a maximum intensity at around 870 ppm and a broader shoulder at lower frequencies, different from the case of the original nanoparticles (without reduction) or that obtained on re-oxidization in oxygen environment (Fig. 5B). The resonance assigned to surface 3-coordinated oxygen ions disappears after reduction. Careful examination of these spectra (inset of Fig. 5B) shows that a broader component is present underneath the resonances of the reduced materials. Fermi Contact (hyperfine) ^{17}O shifts of more than 728 ppm have been observed for oxygen atoms directly bound to the paramagnetic Ce^{3+} ion and similarly large contact shifts are expected in this system.(*31*) We ascribe the broad component to oxygen ions in the first coordination cell of one or more Ce^{3+} ions, the broadening arising from the distribution in local environments and the dipolar interactions between the unpaired electrons centred on Ce^{3+} and ^{17}O.

We have also calculated the chemical shifts of the environments generated by the presence of the Ce^{3+} ions and oxygen vacancies and the observation of a sharper peak at a lower frequency is supported by DFT calculations. Three models constructed to describe the reduced ceria were considered: (i) CeO_2 (2×2×2) unit cell with an oxygen vacancy, which represents the situation of bulk oxygen vacancy; (ii) CeO_2(111) with a sub-surface oxygen vacancy; and (iii) CeO_2(111) with a surface oxygen vacancy, both models (ii) and (iii) representing the situation of vacancies near the surface. All the three models contain the two Ce^{3+} ions required to create one oxygen vacancy. The structures of the three models are shown in Fig. S17A-C and the calculated chemical shifts are summarized in Fig. S17D-F and Table S6-8. Generally, the calculated chemical shifts for the oxygen ions 5 Å or less away from the oxygen vacancy in model (i) show a slightly smaller chemical shift compared to the 877 ppm resonance in bulk CeO_2; similar trends are observed for oxygen ions close to a vacancy (i.e., in the same layer or the next layer to the oxygen vacancy). The oxygen ions further away show a chemical shift around 877 ppm. The

average chemical shift for the oxygen ions close to an oxygen vacancy is approximately 845 ppm in the three different structural models. Note that we have not included the additional hyperfine shifts that will result from the presence of the Ce^{3+} ions since these cannot be readily calculated and so have only considered the environments that are not in the Ce^{3+} 1st shell.

Discussion

In conclusion, this paper describes a novel ^{17}O NMR approach to study the surface and defect sites of nanosized oxides. Since the oxygen ions on the surface of ceria nanoparticles (1st, 2nd and 3rd surface layers) show very distinct chemical shift compared to those in the bulk, ^{17}O NMR spectroscopy can be a sensitive probe to monitor the local structure of oxide nanocrystals. Adsorbing water on ceria can be used to explicitly label oxygen ions in the very top surface layers (1st and 2nd), the method being more controlled than simply heating the nanoparticles at high temperatures. Thus the method allows for inexpensive ^{17}O enrichment of the surface sites of nanostructures, enabling the most active species to be identified and their fate in a chemical reaction to be followed conveniently. Double resonance NMR techniques can be used to distinguish hydroxyl groups from other surface sites. These methods provide a new strategy to study the unique local structure and surface chemistry of nanostructured oxides, as well as their performance in a wide range of applications. Moreover, we expect this approach can be used to study the interfaces between oxides and other materials, and illuminate important issues such as the nature of the interactions between the catalytic active species and the support oxides[*(32)*], and the differences in anionic conductivity that are often seen at the interface between two oxides[*(33)*].

Although the new approach presented allows the detection of the evolution of oxygen species in a chemical process, the exchange of oxygen ions (e.g., the process shown in Fig. 4) may limit its applications in monitoring the behaviours of oxygen ions in reactions at elevated temperature.

Materials and Methods

Study Design.

The sizes of ceria nanoparticles were determined with the XRD data by using Debye-Scherrer equation, which were in general agreement with the surface area measurements. There is no rule for stopping NMR data collection in advance and data acquisition was stopped when enough signal/noise ratio was achieved. Each experimental measurement (sample preparations and NMR experiments) was repeated at least once to ensure that the results can be replicated.

Materials preparation.

Preparations of ceria nanoparticles. $(NH_4)_2Ce(NO_3)_6$ (1.645 g, 3 mmol, Sinopharm Chemical Reagent Co., Ltd) was dissolved in distilled water (50 mL) and the mixture was stirred magnetically for 10 min to obtain a good homogeneity. The solution was then transferred into an 80 mL autoclave, and heated at 393 K under autogenous pressure for 10 h before it was allowed to cool down to room temperature. The resulting light-yellow precipitates were washed with distilled water and anhydrous enthanol 4 times, and then dried at 353 K for 12 h.

Preparations of ceria nanorods. The synthesis of CeO_2 nanorods followed the procedure of Mai et al[(34)]. In a typical preparation procedure, 1.96 g $Ce(NO_3)_3 \cdot 6H_2O$ was dissolved in 40 mL ultrapure water (resistance>18 MW), and 16.88 g NaOH was dissolved in 30 mL ultrapure water. The NaOH solution was added dropwise into the $Ce(NO_3)_3$ solution under magnetic stirring at room temperature (RT). The solution was stirred for an additional 30 min at RT and then transferred into a 100 mL Teflon bottle, which was tightly sealed and hydrothermally treated in an autoclave at 373 K for 24 h before cooling to RT. The resulting white precipitate was collected, washed with ultrapure water, and dried under vacuum at 353 K for 16 h. After that, the acquired yellow powder was calcined at 973 K for 4 h to obtain CeO_2 nanorods.

^{17}O enrichment procedures.

Bulk ceria (typically 200 mg, Sinopharm Chemical Reagent Co., Ltd) and nanosized ceria (typically 200 mg) were first heated at 573 K for 10 h (except the ceria nanoparticles which were later enriched at 523 K, this particular sample was heated at 523 K) and then enriched by heating the powders in an 70 % ^{17}O enriched O_2 gas (Cambridge Isotope Laboratories) atmosphere at various temperatures (523 ~ 1073 K) for 10 h (for "bulk" ceria sample, ^{17}O enrichment was performed at 1073 K for 10 h). Ceria nanoparticles were also enriched via the introduction of a small amount of 70 % ^{17}O enriched H_2O (Cambridge Isotope Laboratories) by first adding water dropwise or introducing water using a vacuum line at room temperature then exposing the samples to vacuum to remove additional water. For introducing water using a vacuum line, water vapor (typically 0.1 mmol) was adsorbed onto ceria samples (typically 200 mg) at room temperature for 5 min.

Hydrogen reduction.

Ceria samples (typically 200 mg) were reduced under hydrogen (1 bar) in a sealed quartz tube at 773 K for 5 min before allowing them to cool to room temperature under vacuum.

Solid state NMR spectroscopy.

^{17}O MAS NMR spectra were performed on 9.4 and 14.1 T Bruker Avance III spectrometers using 1.3 mm HXY, 3.2 mm HXY, and 4 mm HXY MAS probes (in double resonance) tuned to ^{17}O at 54.2 and 81.3 MHz, respectively. Ultrahigh field data were collected on a 19.6 T Bruker DRX spectrometer using a 1.8 mm single channel probe tuned to 112.9 MHz. All the samples were packed into the rotors in the N_2 glove box unless otherwise stated. ^{17}O chemical shift is referenced to H_2O at 0.0 ppm.

DFT calculations.

The spin-polarized calculations were carried out with the GGA-PBE functional using the Vienna *ab initio* Simulation Package (VASP)[*(35)*], which can calculate chemical shifts for

crystalline systems using the linear response method and electric field gradients (EFG) at the positions of the atomic nuclei. The project-augmented wave method (PAW)[36] was used to describe the electron-core interaction. The Ce (5s, 5p, 6s, 5d, 4f), O (2s, 2p) and H (1s) shells were treated as valence electrons. We used a plane wave kinetic energy cutoff of 500 eV for structure optimization, chemical shift and EFG calculations. All atoms were allowed to move and the structural relaxing calculations were converged until the Hellman-Feynman forces on each ion were less than 0.02 eV/Å. For chemical shift and EFG calculations, we used a typically higher stopping-criterion of 10^{-8} eV for electronic minimization (Fig. S18A). Particularly, to characterize the electronic and geometric structures of ceria properly, we added a Hubbard U of 5 eV suggested by Nolan and co-workers[37] in DFT calculations. Using the PBE+U method, we obtained a lattice parameters of 5.448 Å for bulk ceria, which is in good agreement with the experiment value (5.411 Å)[38]. The {111}, {110} and {100} facets of CeO_2 were modeled by surface slabs which are thick enough to maintain trivial fluctuations of chemical shift values in their middle layers, and they were all represented by p(2×2) lateral cells (Fig. S6A-C). For CeO_2(100), we removed half of the oxygen atoms from the outermost planes to offset the net dipole and make it stable. To avoid interactions between slabs, they were separated by a vacuum gap greater than 10 Å. The Brillouin-zone integration was performed using a 2×2×1 and 1×1×1 Monkhorst-Pack grid for surface slabs and the (2×2×2) bulk cell, respectively. The isotropic chemical shift (δ_{iso}) is defined as, $\delta_{iso} = \delta_{ref} + m\delta_{cal}$ where δ_{ref} is the reference chemical shift (Fig. S18B), m is a gradient assumed equal to -1, and δ_{cal} is the chemical shift value obtained within VASP. The quadrupole coupling constant (C_Q) was calculated as $C_Q = \frac{eQV_{zz}}{h}$ where e is the absolute value of the electron charge, Q is the element and isotope specific quadrupole moment (the experimental value of Q=-0.02558 barns[39] is used for the ^{17}O), V_{ii} is the eigenvalues of the EFG tensor ($|V_{zz}| > |V_{yy}| > |V_{xx}|$), h is the Planck constant.

A chemical shift calculation of clean CeO_2(111) surface was performed without structure relaxing (Fig. S18B). The results show that the chemical shifts of oxygen atoms at 5^{th}~8^{th} O layers have a constant value of 825 ppm. Considering that the bulk oxygen ions have more regular arrangements than the oxygen ions near the surfaces, thus this constant value can be used to estimate the reference chemical shift value (δ_{ref}). As a result, 52 ppm was taken as the δ_{ref} ($\delta_{ref} = \delta_{iso}(bulk) - m \times \delta_{cal}(bulk) = 877$ ppm $- 1 \times 825$ ppm $= 52$ ppm).

Supplementary Materials

References and Notes

1. T. J. Bastow, S. N. Stuart, ^{17}O NMR in simple oxides. *Chem. Phys.* **143**, 459-467 (1990).
2. S. Yang, K. D. Park, E. Oldfield, Oxygen-17 labeling of oxides and zeolites. *J. Am. Chem. Soc.* **111**, 7278-7279 (1989).
3. K. J. D. MacKenzie, M. E. Smith, *Multinuclear Solid-State Nuclear Magnetic Resonance of Inorganic Materials*. (ELSEVIER, Kidlington, Oxford, UK, 2002), vol. 6.
4. S. E. Ashbrook, M. E. Smith, Solid state ^{17}O NMR-an introduction to the background principles and applications to inorganic materials. *Chem. Soc. Rev.* **35**, 718-735 (2006).

5. E. Scolan, C. Magnenet, D. Massiot, C. Sanchez, Surface and bulk characterisation of titanium-oxo clusters and nanosized titania particles through ^{17}O solid state NMR. *J. Mater. Chem.* **9**, 2467-2474 (1999).

6. A. V. Chadwick, I. J. F. Poplett, D. T. S. Maitland, M. E. Smith, Oxygen speciation in nanophase MgO from solid-state ^{17}O NMR. *Chem. Mater.* **10**, 864-870 (1998).

7. P. G. Bruce, B. Scrosati, J.-M. Tarascon, Nanomaterials for Rechargeable Lithium Batteries. *Angew. Chem. Int. Ed.* **47**, 2930-2946 (2008).

8. A. T. Bell, The Impact of Nanoscience on Heterogeneous Catalysis. *Science* **299**, 1688-1691 (2003).

9. P. Seungdoo, J. M. Vohs, Direct oxidation of hydrocarbons in a solid-oxide fuel cell. *Nature* **404**, 265 (2000).

10. J. A. Rodriguez, S. Ma, P. Liu, J. Hrbek, J. Evans, M. Perez, Activity of CeO_x and TiO_x nanoparticles grown on Au(111) in the water-gas shift reaction. *Science* **318**, 1757-1760 (2007).

11. J. Kašpar, P. Fornasiero, M. Graziani, Use of CeO_2-based oxides in the three-way catalysis. *Catal. Today* **50**, 285-298 (1999).

12. R. W. Tarnuzzer, J. Colon, S. Patil, S. Seal, Vacancy Engineered Ceria Nanostructures for Protection from Radiation-Induced Cellular Damage. *Nano Lett.* **5**, 2573-2577 (2005).

13. C. Tyrsted, K. M. Jensen, E. D. Bojesen, N. Lock, M. Christensen, S. J. Billinge, B. Brummerstedt Iversen, Understanding the formation and evolution of ceria nanoparticles under hydrothermal conditions. *Angew. Chem. Int. Ed.* **51**, 9030-9033 (2012).

14. K. Zhou, X. Wang, X. Sun, Q. Peng, Y. Li, Enhanced catalytic activity of ceria nanorods from well-defined reactive crystal planes. *J. Catal.* **229**, 206-212 (2005).

15. Y. Jiang, J. B. Adams, M. van Schilfgaarde, Density-functional calculation of CeO_2 surfaces and prediction of effects of oxygen partial pressure and temperature on stabilities. *J. Chem. Phys.* **123**, 064701 (2005).

16. N. Kim, J. F. Stebbins, Vacancy and cation distribution in yttria-doped ceria: An ^{89}Y and ^{17}O MAS NMR study. *Chem. Mater.* **19**, 5742-5747 (2007).

17. S. Tsunekawa, R. Sivamohan, S. Ito, A. Kasuya, T. Fukuda, Structural study on monosize CeO_{2-X} nano-particles. *Nanostruct. Mater.* **11**, 141-147 (1999).

18. S. Cadars, B. J. Smith, J. D. Epping, S. Acharya, N. Belman, Y. Golan, B. F. Chmelka, Atomic Positional Versus Electronic Order in Semiconducting ZnSe Nanoparticles. *Phys. Rev. Lett.* **103**, 136802 (2009).

19. X. Xie, Y. Li, Z. Q. Liu, M. Haruta, W. Shen, Low-temperature oxidation of CO catalysed by Co_3O_4 nanorods. *Nature* **458**, 746-749 (2009).

20. A. Badri, C. Binet, J.-C. Lavalley, An FTIR study of surface ceria hydroxy groups during a redox process with H_2. *J. Chem. Soc., Faraday Trans.* **92**, 4669-4673 (1996).

21. A. Pines, M. G. Gibby, J. S. Waugh, Proton-enhanced NMR of dilute spins in solids. *J. Chem. Phys.* **59**, 569-590 (1973).

22. T. Gullion, J. Schaefer, Rotational-Echo, Double-Resonance NMR. *J. Magn. Reson.* **81**, 196-200 (1989).

23. L. M. Peng, Y. Liu, N. J. Kim, J. E. Readman, C. P. Grey, Detection of Bronsted acid sites in zeolite HY with high-field ^{17}O-MAS-NMR techniques. *Nature Mater.* **4**, 216-219 (2005).

24. L. Zhao, Z. Qi, F. Blanc, G. Yu, M. Wang, N. Xue, X. Ke, X. Guo, W. Ding, C. P. Grey, L. Peng, Investigating Local Structure in Layered Double Hydroxides with ^{17}O NMR Spectroscopy. *Adv. Funct. Mater.* **24**, 1696-1702 (2014).

25. N. Merle, J. Trebosc, A. Baudouin, I. D. Rosal, L. Maron, K. Szeto, M. Genelot, A. Mortreux, M. Taoufik, L. Delevoye, R. M. Gauvin, ^{17}O NMR gives unprecedented insights

into the structure of supported catalysts and their interaction with the silica carrier. *J. Am. Chem. Soc.* **134**, 9263-9275 (2012).

26. J. Spanier, R. Robinson, F. Zhang, S.-W. Chan, I. Herman, Size-dependent properties of CeO_{2-y} nanoparticles as studied by Raman scattering. *Phys. Rev. B* **64**, 245407 (2001).

27. S. Deshpande, S. Patil, S. V. N. T. Kuchibhatla, S. Seal, Size dependency variation in lattice parameter and valency states in nanocrystalline cerium oxide. *Appl. Phys. Lett.* **87**, 133113 (2005).

28. J. Światowska, V. Lair, C. Pereira-Nabais, G. Cote, P. Marcus, A. Chagnes, XPS, XRD and SEM characterization of a thin ceria layer deposited onto graphite electrode for application in lithium-ion batteries. *Appl. Surf. Sci.* **257**, 9110-9119 (2011).

29. T. Kayama, K. Yamazaki, H. Shinjoh, Nanostructured Ceria−Silver Synthesized in a One-Pot Redox Reaction Catalyzes Carbon Oxidation. *J. Am. Chem. Soc.* **132**, 13154-13155 (2010).

30. M. Boaro, M. Vicario, C. de Leitenburg, G. Dolcetti, A. Trovarelli, The use of temperature-programmed and dynamic/transient methods in catalysis: characterization of ceria-based, model three-way catalysts. *Catal. Today* **77**, 407-417 (2003).

31. K. Djanashvili, C. Platas-Iglesias, J. A. Peters, The structure of the lanthanide aquo ions in solution as studied by ^{17}O NMR spectroscopy and DFT calculations. *Dalton Trans.* , 602-607 (2008).

32. J. A. Farmer, C. T. Campbell, Ceria maintains smaller metal catalyst particles by strong metal-support bonding. *Science* **329**, 933-936 (2010).

33. J. Garcia-Barriocanal, A. Rivera-Calzada, M. Varela, Z. Sefrioui, E. Iborra, C. Leon, S. J. Pennycook, J. Santamaria, Colossal ionic conductivity at interfaces of epitaxial ZrO_2:Y_2O_3/$SrTiO_3$ heterostructures. *Science* **321**, 676-680 (2008).

34. H.-X. Mai, L.-D. Sun, Y.-W. Zhang, R. Si, W. Feng, H.-P. Zhang, H.-C. Liu, C.-H. Yan, Shape-Selective Synthesis and Oxygen Storage Behavior of Ceria Nanopolyhedra, Nanorods, and Nanocubes. *J. Phys. Chem. B* **109**, 24380-24385 (2005).

35. G. Kresse, J. Hafner, Ab initio molecular-dynamics simulation of the liquid-metal–amorphous-semiconductor transition in germanium. *Phys. Rev. B* **49**, 14251-14269 (1994).

36. P. E. Blöchl, Projector augmented-wave method. *Phys. Rev. B* **50**, 17953-17979 (1994).

37. M. Nolan, S. Grigoleit, D. C. Sayle, S. C. Parker, G. W. Watson, Density functional theory studies of the structure and electronic structure of pure and defective low index surfaces of ceria. *Surf. Sci.* **576**, 217-229 (2005).

38. E. A. Kümmerle, G. Heger, The Structures of C–$Ce2O_{3+\delta}$, Ce_7O_{12}, and $Ce_{11}O_{20}$. *J. Solid State Chem.* **147**, 485-500 (1999).

39. D. Sundholm, J. Olsen, Finite element multiconfiguration Hartree-Fock calculations on carbon, oxygen, and neon: the nuclear quadrupole moments of ^{11}C, ^{17}O, and ^{21}Ne. *J. Phys. Chem*. **96**, 627-630 (1992).

Acknowledgments:

General: We thank Dr. Pan Shi, Prof. Changlin Tian (High Magnetic Field Laboratory, Chinese Academy of Sciences), and Dr. Xuefeng Wang, Prof. Xiuwen Han, Prof. Xinhe Bao (Dalian Institute of Chemical Physics, Chinese Academy of Sciences) for the help with high field NMR experiments. We also thank Dr. Junjian Miao and Prof. Shuhua Li (School of Chemistry and Chemical Engineering, Nanjing University) for the help with DFT calculations. **Funding:** This work was supported by the National Basic Research Program of China (2013CB934800, 2011CB808505), the National Natural Science Foundation of China (NSFC) (20903056,

21222302, 21322307 and 21073083), NSFC - Royal Society Joint Program (21111130201), Program for New Century Excellent Talents in University (NCET-10-0483), the Fundamental Research Funds for the Central Universities (1124020512) and National Science Fund for Talent Training in Basic Science (J1103310). The ECUST group also thanks the Shanghai Rising-Star Program (12QH1400700) and National Super Computing Centre in Jinan for computing time. F.B. thanks the EU Marie Curie actions for an International Incoming fellowship 2011-2013 (Grant No. 275212), Clare Hall, University of Cambridge, UK for a Research fellowship and the University of Liverpool, UK for funding. C.P.G. thanks the European Research Council for an Advanced Fellowship. This work was also supported by a Project Funded by the Priority Academic Program Development of Jiangsu Higher Education Institutions. **Author contributions:** M.W., S.Z., L.Z., Y.G. and W.H. carried out the synthesis of ceria nanostructures. M.W., L.L., N.X. and X.G. carried out XRD, electron microscopy, surface area measurement and other characterizations; M.W., S.Z., L.Z., L.S. and L.P. performed ^{17}O isotope enrichment, collected and analysed the NMR spectra; M.W., Z.Y., Z.G., F.B. and X.K. collected and analysed the high field NMR spectra; X.-P.W., and X.-Q.G. conducted the DFT calculations; M.W., X.-P.W., W.H., W.D., X.-Q.G., C.P.G. and L.P. wrote the manuscript and all authors discussed the experiments and final manuscript. **Competing interests:** The authors declare no competing financial interests.

Figures and Tables

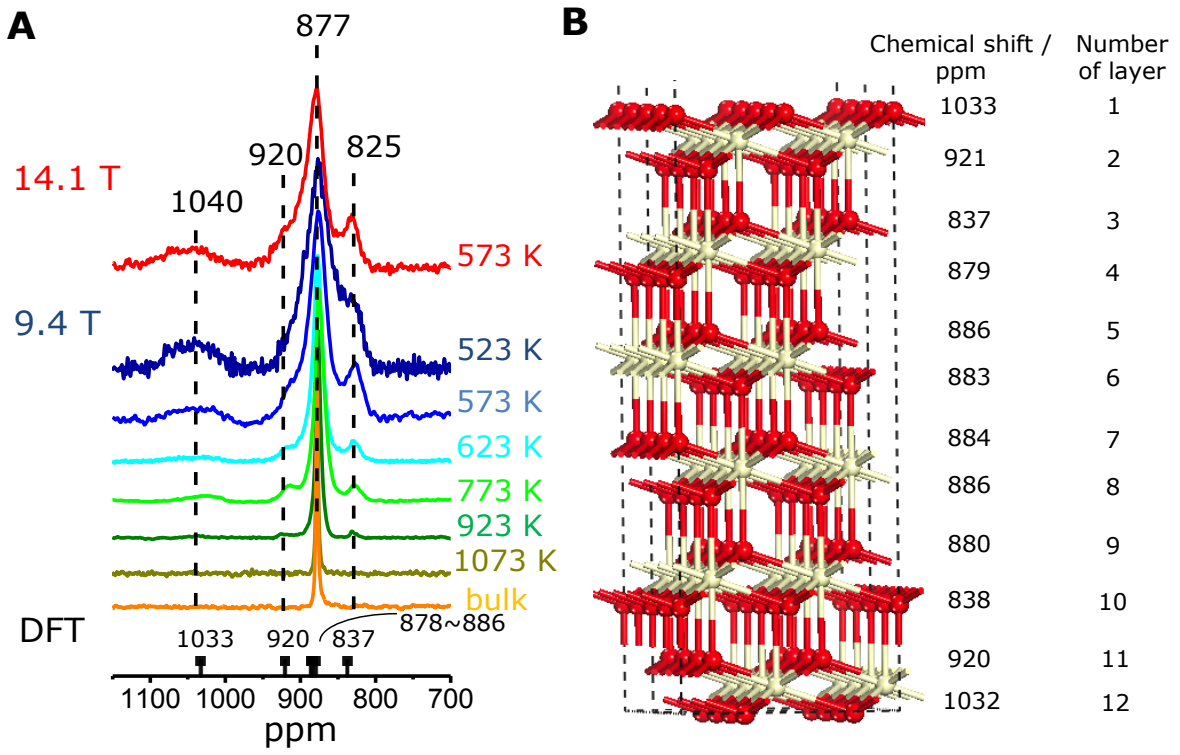

Fig. 1. Solid state NMR spectra of nanosized ceria in comparison with DFT calculations. (**A**), ^{17}O NMR spectra for ceria nanoparticles enriched at different temperatures and external fields compared with the ^{17}O NMR spectra of micron-sized ceria ("bulk" ceria) and the summary of the chemical shifts predicted using a structural model shown in b. The spectra obtained at 14.1 and 9.4 T were acquired with spinning speeds of 55 and 20 kHz, respectively. Short pulse lengths of 0.1 ~ 0.4 μs corresponding to π/72 ~ π/18 pulses for $H_2{}^{17}O$ and optimized recycle delays from 1 ~ 100 s to ensure quantitative observations of all the resonances were used. Detailed experimental parameters are summarized in Table S9. (**B**),The structural model of ceria used in the DFT calculations. Red and white spheres represent oxygen and cerium ions, respectively. The exposed surface is (111) and the calculated chemical shift of ^{17}O in each layer is shown on the right side.

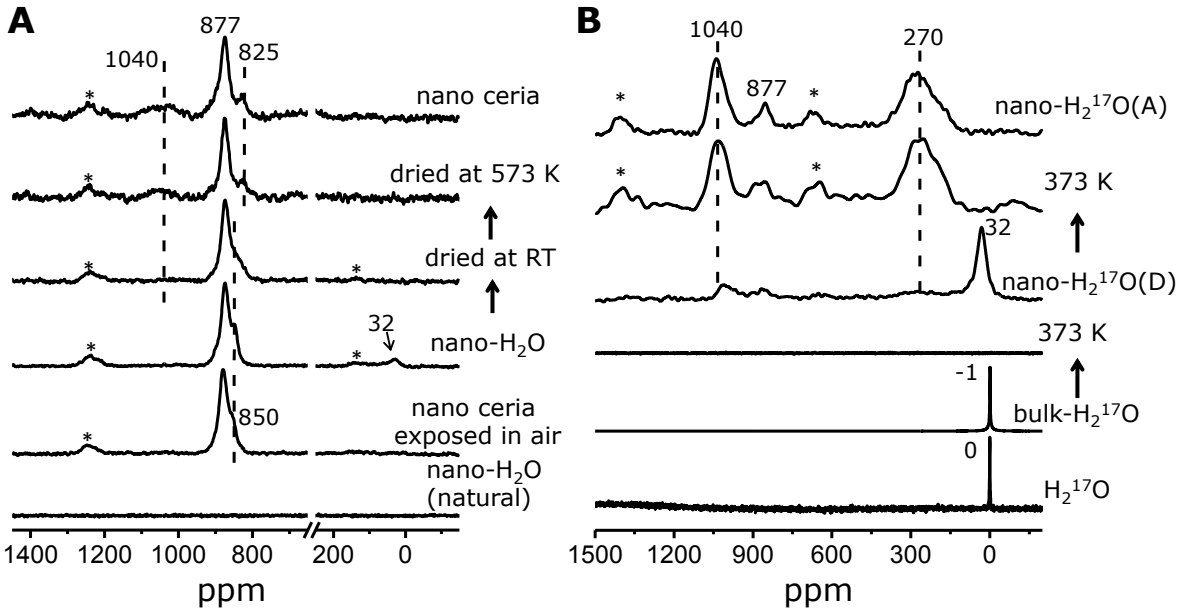

Fig. 2. Solid state NMR spectra of ceria in contact with water. (**A**), (from bottom to top) ^{17}O MAS NMR spectra of non-enriched ceria nanoparticles adsorbed with non-enriched water; ceria nanoparticles enriched in $^{17}O_2$ at 573 K then exposed to air; ceria nanoparticles enriched in $^{17}O_2$ at 573 K then adsorbed with non-enriched water (water was added dropwise); the previous sample dried under vacuum at room temperature; and at 573 K; and ceria nanoparticles enriched in $^{17}O_2$ at 573 K. (**B**), (from bottom to top) ^{17}O NMR spectra of liquid $H_2{}^{17}O$; ^{17}O MAS NMR spectra of bulk ceria adsorbed with $H_2{}^{17}O$ (bulk- $H_2{}^{17}O$); the previous sample dried under vacuum at 373 K; non-enriched ceria nanoparticles adsorbed with $H_2{}^{17}O$ by adding water dropwise (nano- $H_2{}^{17}O$(D)); the previous sample dried under vacuum at 373 K; and non-enriched ceria nanoparticles adsorbed with $H_2{}^{17}O$ by adsorbing water through vacuum line and then dried under vacuum at 373 K (nano- $H_2{}^{17}O$(A)). The samples of $H_2{}^{17}O$, bulk- $H_2{}^{17}O$ and nano- $H_2{}^{17}O$(D) in (b) were packed into the rotors in air. All the spectra were acquired at 9.4 T. Detailed experimental parameters are summarized in Table S10. Asterisks "∗" denotes spinning sidebands.

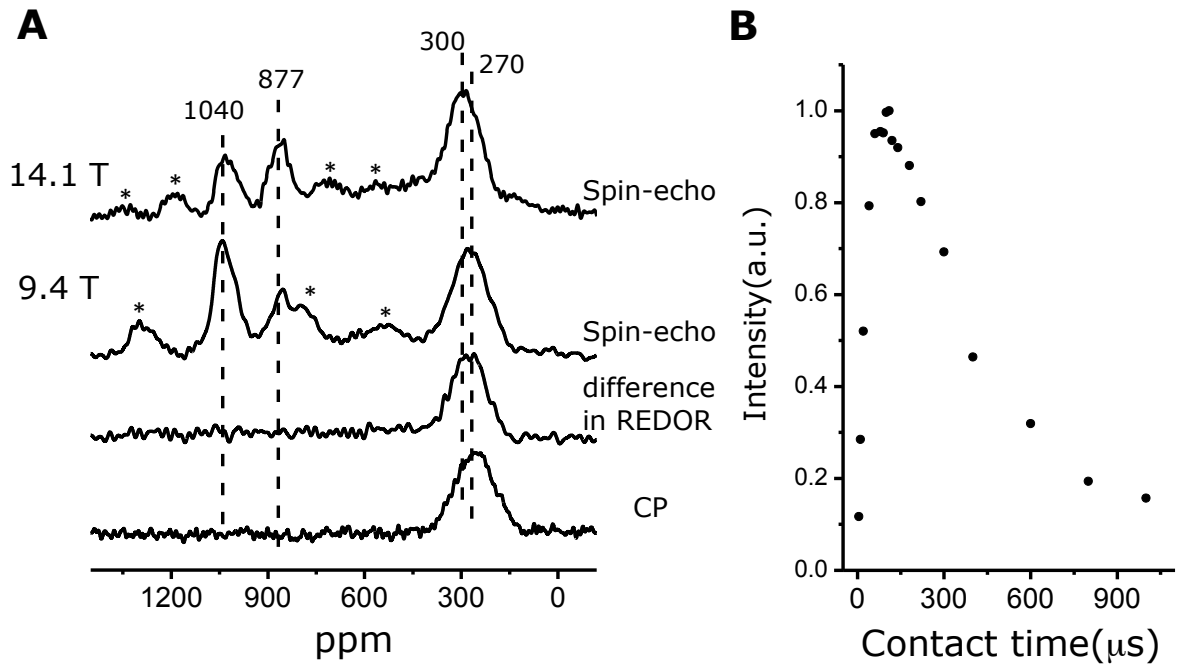

Fig. 3. Double resonance solid state NMR data of ceria nanoparticles. (**A**), (from top to bottom) ^{17}O MAS NMR spectra of ceria nanoparticles adsorbed with ^{17}O water followed by thermal treatment under vacuum at 373 K at 14.1 and 9.4 T; difference spectrum in ^{17}O-^{1}H REDOR experiments; and ^{1}H-^{17}O CP MAS NMR spectrum with a contact time of 100 μs. (**B**), The peak intensity in CP MAS NMR experiment as a function of contact time. Spectra were obtained at both 9.4 and 14.1 T under MAS rates of 13 ~ 14 kHz. 1,000 ~ 40,000 scans were averaged and recycle delays from 0.2 ~ 1 s were used. Asterisks "∗" denotes spinning sidebands.

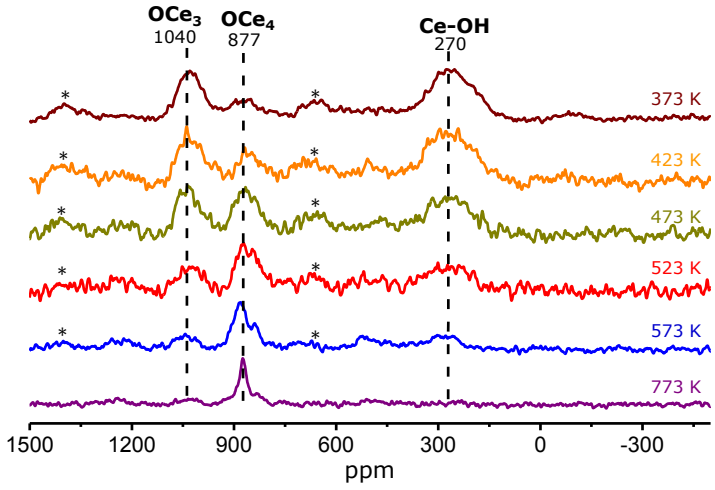

Fig. 4. Solid state NMR spectra of ceria nanoparticles adsorbed with $H_2{}^{17}O$ followed by thermal treatment. From top to bottom, ^{17}O NMR spectrum of non-enriched ceria nanoparticles adsorbed with $H_2{}^{17}O$ by adding water dropwise, then dried under vacuum at 373, 423, 473, 523, 573 and 773 K. A rotor synchronized Hahn-echo sequence ($\pi/6$ - τ - $\pi/3$- τ - acquisition) was used. Spectra were obtained at 9.4 T under a MAS rate of 20 kHz. 8,000 ~ 20,000 scans were collected and recycle delays from 0.2 ~ 0.5 s were used. Asterisks "*" denotes spinning sidebands.

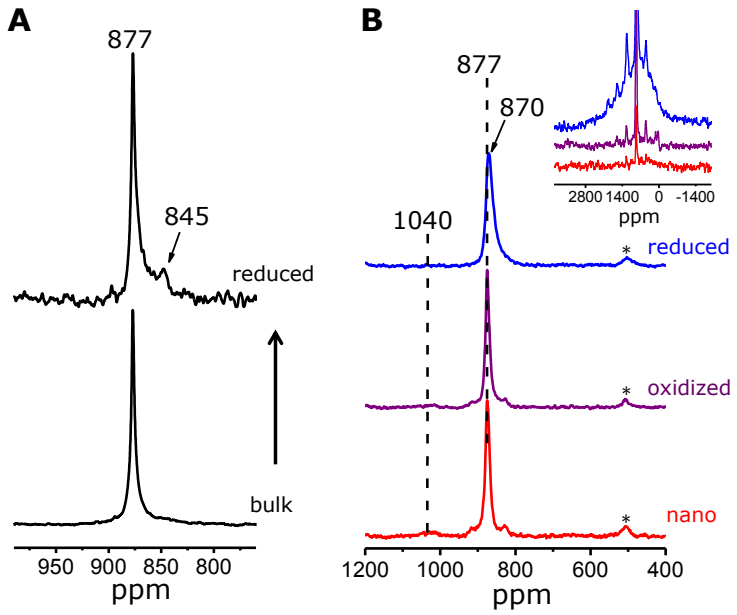

Fig. 5. Solid state NMR spectra of reduced ceria in comparison with bulk and nanosized ceria. (**A**), ^{17}O NMR spectra of bulk ceria enriched in $^{17}O_2$ at 1073 K (bottom) and reduced in H_2 atmosphere at 1073 K (top). (**B**), ^{17}O NMR spectra of nanosized ceria enriched in $^{17}O_2$ at 773 K (bottom), reduced in H_2 atmosphere at 773 K (top), and re-oxidized in air reduced ceria (middle). Inset shows the full width of the three ^{17}O spectra. A rotor synchronized Hahn-echo sequence ($\pi/6 - \tau - \pi/3 - \tau$ - acquisition) was used. Data were obtained at 9.4 T under a MAS rate of 20 kHz. 100,000 (a, bulk), 300,000 (a, reduced), 1024 (b) and 40,000 scans (b, inset) were averaged and recycle delays of 0.1 s (a), 1 s (b) and 0.01 s (b, inset) were used. Asterisks "∗" denotes spinning sidebands.

Supplementary Materials

Materials and Methods

Characterization: X-Ray Diffraction (XRD) patterns of prepared samples were recorded in the 2θ region of 5 - 90° on a Philips X'Pert X-ray diffractometer with a Cu Kα radiation (40 kV, 40 mA, λ = 1.5418 Å). TEM micrographs were performed on a JEOL JEM-2010 transmission electron microscope. The Brunauer-Emmett-Teller (BET) specific surface areas of the samples were measured by nitrogen adsorption at 77 K using a Micromeritics tristar ASAP 2020 instrument. The H_2 consumption in TPR experiments was measured by means of a thermal conductivity detector. The reactants (5% hydrogen in nitrogen) were passed over ceria samples with a flow rate of 40 mL/mim. The heating rate was 10 K/min. X-ray photoelectron spectroscopy (XPS) analysis was performed on a PHI 5000 VersaProbe system, using monochromatic Al Kα radiation (1486.6 eV) operating at an accelerating power of 15 kW. Before the measurements, the samples were outgassed at room temperature in a UHV chamber ($<5 \times 10^{-7}$ Pa). The sample charging effects were compensated by calibrating all binding energies (BE) with the adventitious C 1s peak at 284.6 eV. The morphology of the bulk ceria sample was investigated by using a field-emission scanning electron microscope (Hitachi FE-SEM S4800) equipped with an energy dispersive X-ray spectrometer.

The molecular dynamics (MD) simulation and geometry optimization were applied to locate the optimal structure of water/CeO_2(111) interface (Fig. S8). This interface model contains 18 H_2O molecules in vacuum gap (ρ_{water}= 0.98 g/cm^3). A canonical ensemble was used to perform a MD simulation at 300 K for about 16 ps. The top and bottom three atomic layers were relaxed, and other layers were fixed. After that, several low energy structures obtained during the MD simulation were picked out to do geometry optimization. In the end, the structure with lowest

DFT total energy was regarded as the optimal structure of water/CeO_2(111) interface, and the subsequent chemical shift calculation was performed on this structure.

The oxygen vacancy formation energy (E_{ov}) was calculated as $E_{ov}=E_{CeO_{2-\delta}}+\frac{1}{2}E_{O_2}-E_{CeO_2}$ where $E_{CeO_{2-\delta}}$, E_{O_2} and E_{CeO_2} represent the calculated DFT total energies of defective CeO_2(111), gas-phase oxygen and clean CeO_2(111), respectively.

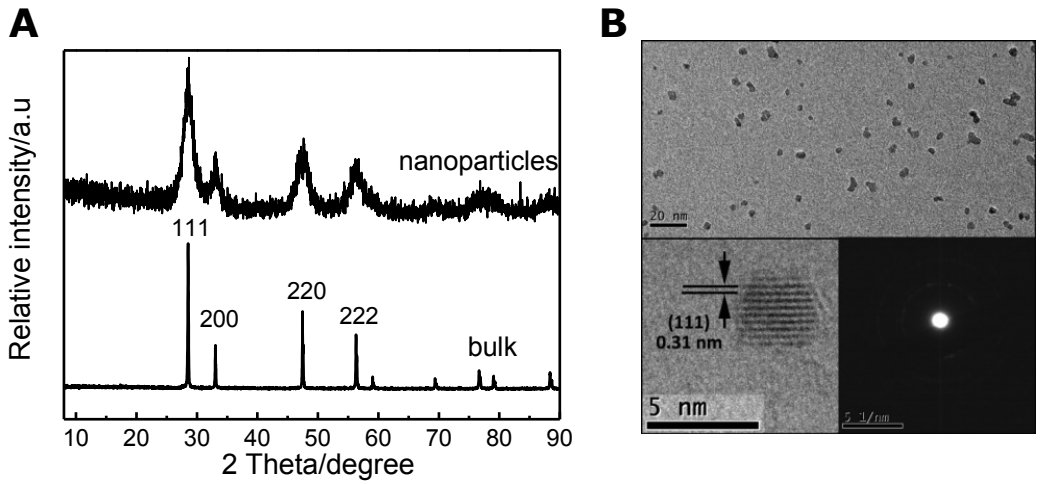

Fig. S1. XRD and electron microscopy characterization of ceria nanoparticles. (A) XRD patterns of ceria nanoparticles and bulk ceria; **(B)** HRTEM images and SAED pattern of ceria nanoparticles.

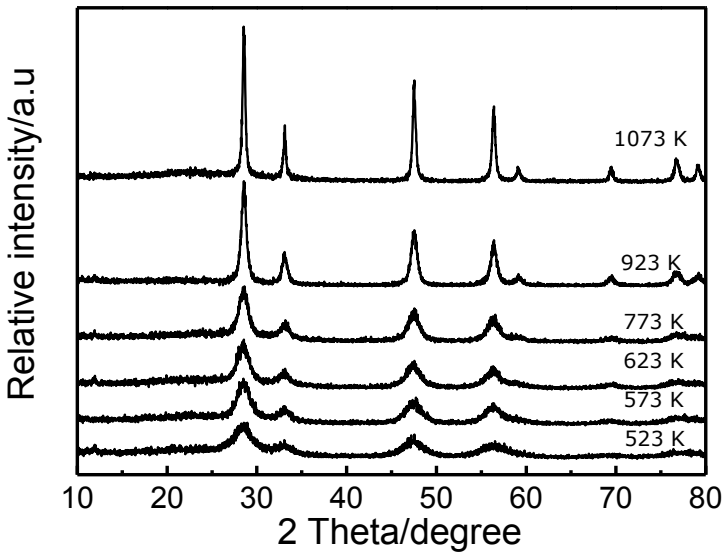

Fig. S2. The XRD patterns of ceria nanoparticles calcined at different temperature.

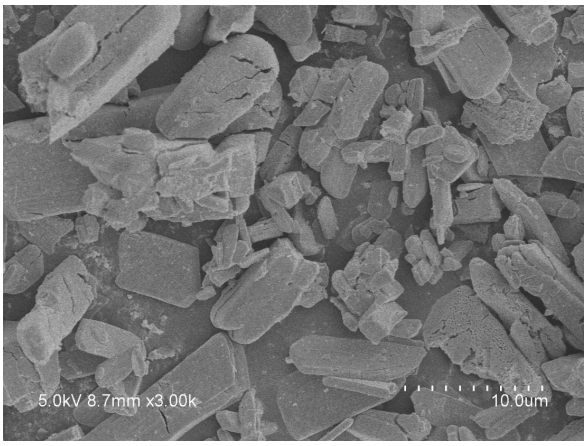

Fig. S3. The SEM image of the bulk ceria sample.

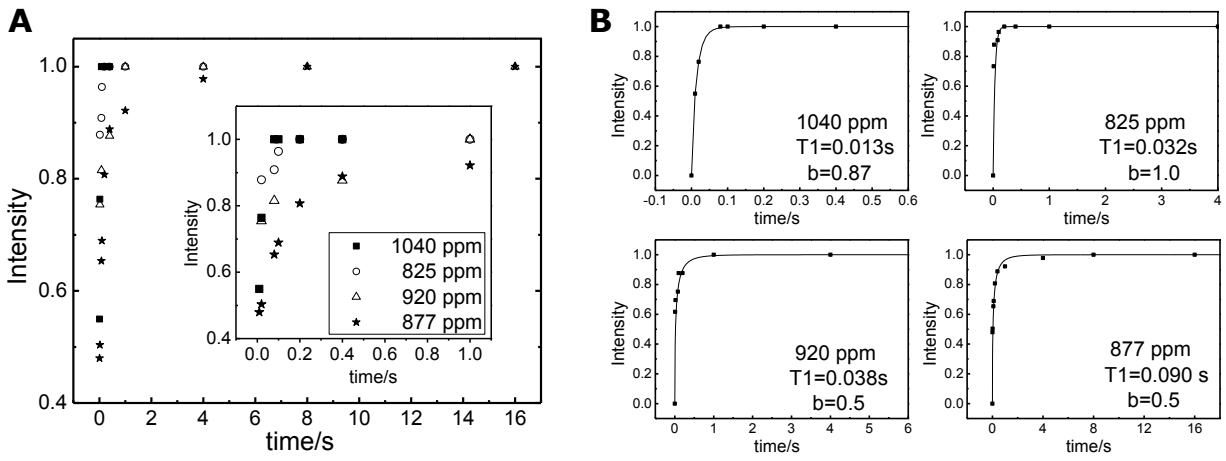

Fig. S4. Longitudinal relaxation studies of ceria nanoparticles. (A) ^{17}O NMR spectra signal intensities measured with different recycle delays on the sample of ceria nanoparticles enriched in $^{17}O_2$ at 573 K using a solution π/18 pulse as the excitation pulse. **(B)** T_1 analytical fits using a stretch exponential function of the type $I(t) = I_0(1 - e^{-(\frac{t}{T_1})^b})$, where $I(t)$ and I_0 are the signal intensities at recycle delay t and at equilibrium, respectively.

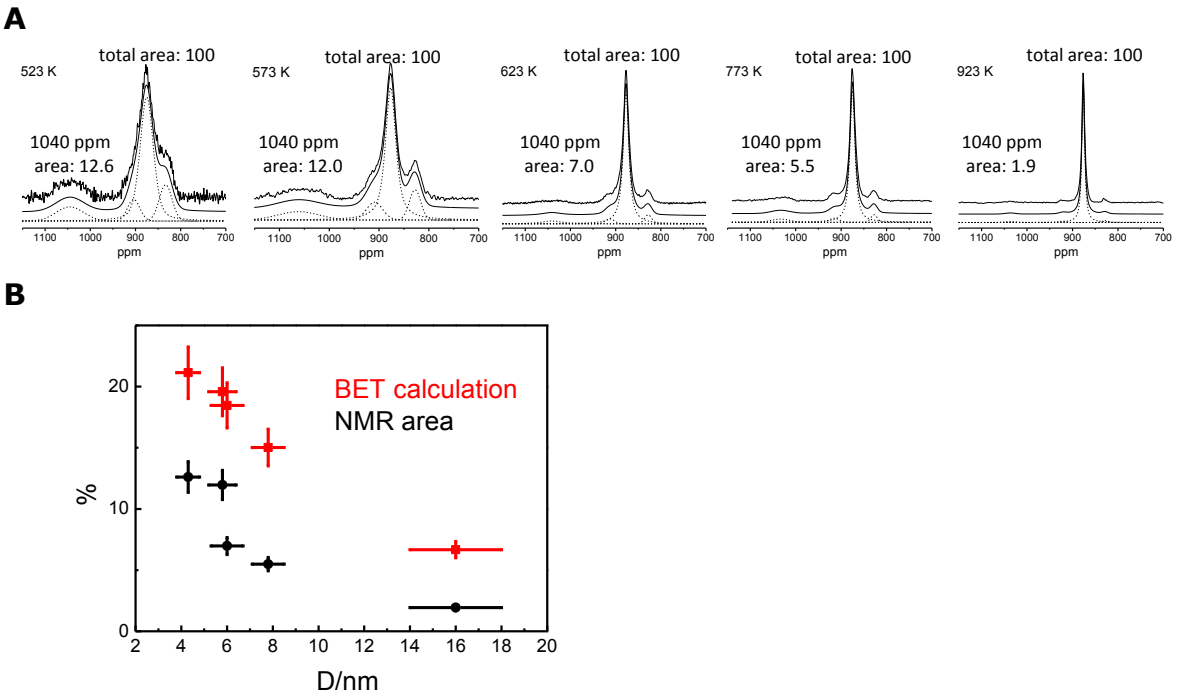

Fig. S5. Quantification of surface oxygen ions from NMR and BET data. (A) ^{17}O NMR spectral deconvolutions for the ceria nanoparticle samples enriched in $^{17}O_2$ at 523, 573, 623, 773 and 923 K, respectively. **(B)** The comparison of the fractions of surface low-coordinated species (~1040 ppm) obtained from spectral deconvolutions **(A)** and estimated according to the BET surface area as a function of the size of nanoparticles.

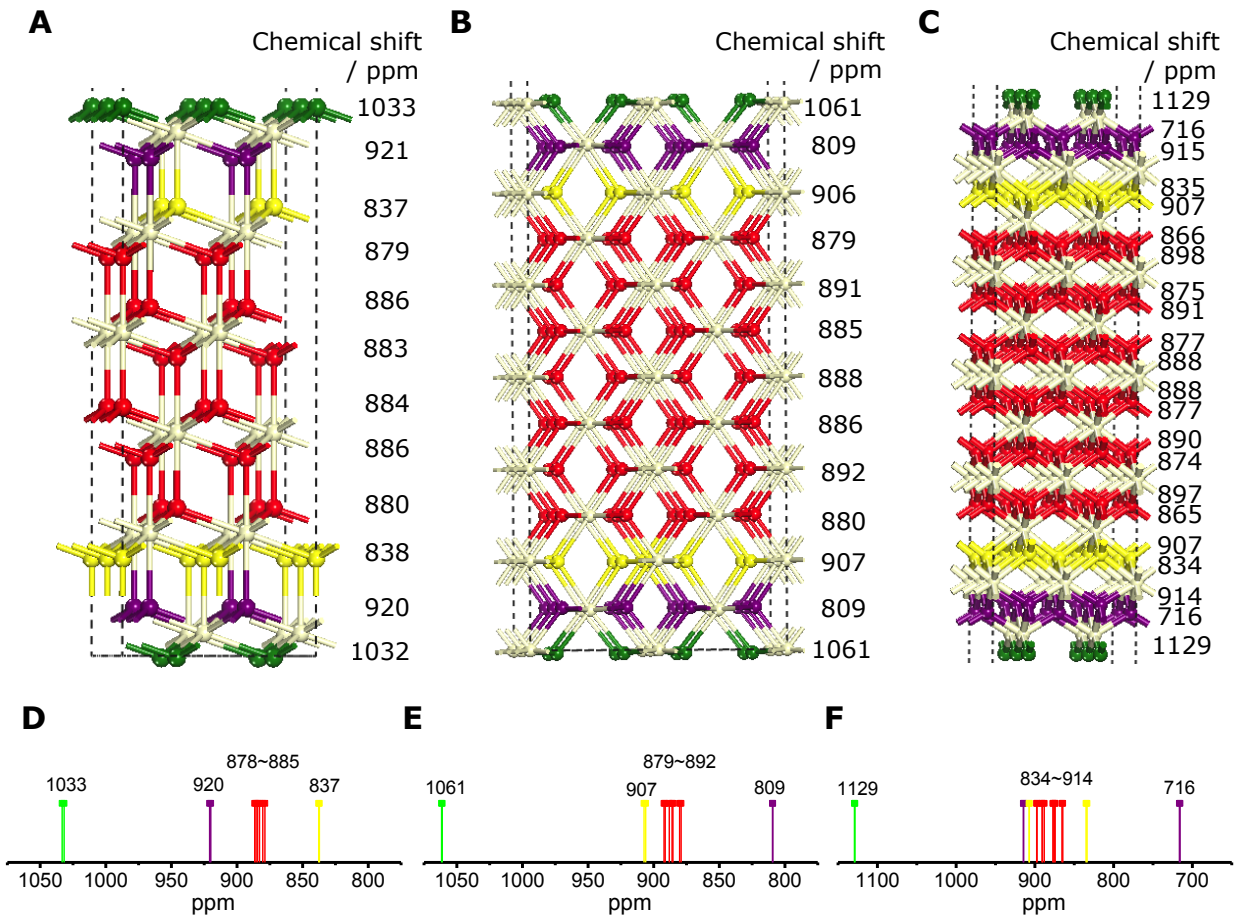

Fig. S6. Chemical shift calculations of ceria with different surface slabs. Calculated CeO_2 (**A**) (111), (**B**) (110) and (**C**) (100) surface slabs, and the summary of the corresponding calculated NMR chemical shifts (**D**, **E** and **F**). 1st, 2nd and 3rd surface layers are in green, violet and yellow, respectively.

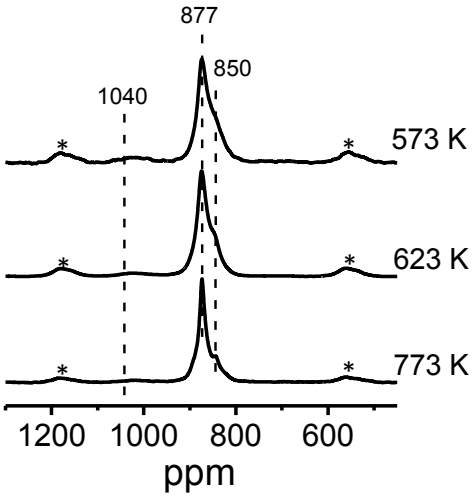

Fig. S7. Solid-state NMR of ceria nanoparticles in contact with water at ultrahigh field. ^{17}O MAS NMR spectra of nanosized ceria enriched in $^{17}O_2$ at different temperatures in contact with water at ultrahigh external field of 19.4 T. The samples were packed into the rotors in air. A rotor synchronized Hahn-echo sequence ($\pi/2$ - τ - π- τ - acquisition) was used. Spinning speed, 35 kHz; recycle delays, 1 s; number of scans, 3,000 ~ 10,000. "*" denotes spinning sidebands.

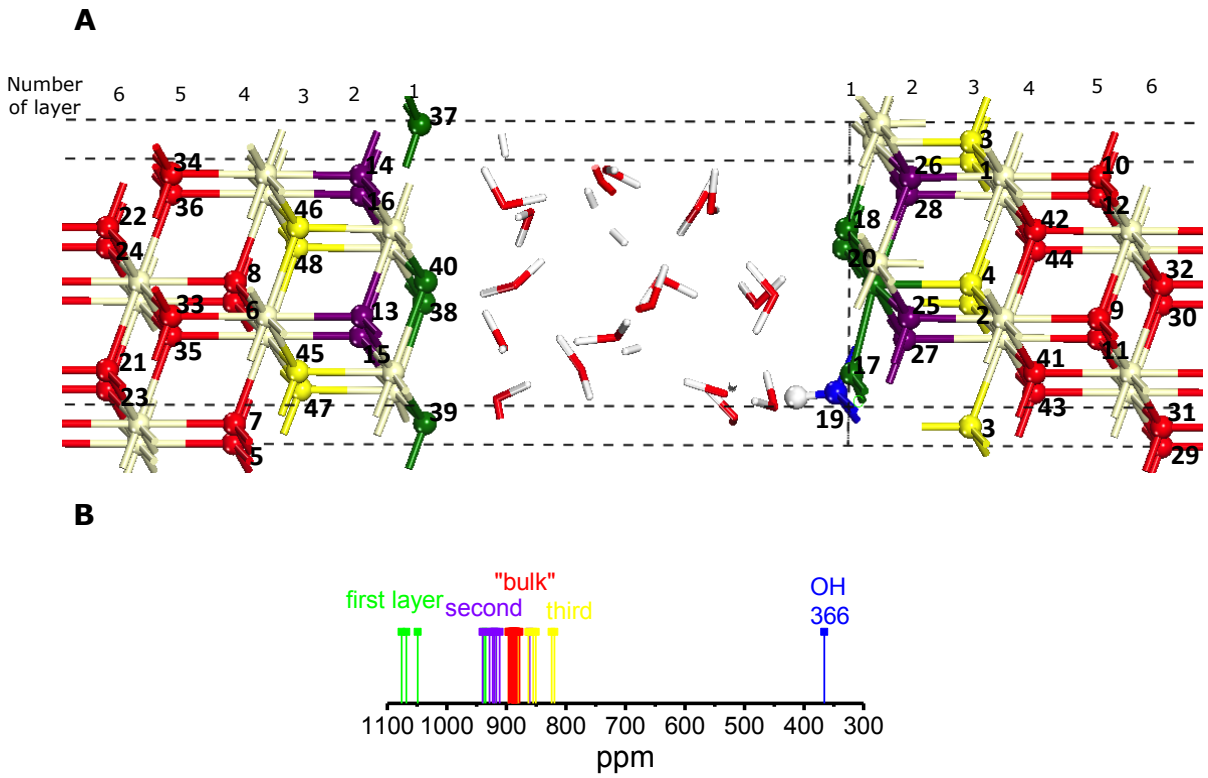

Fig. S8. DFT calculations for ceria in contact with water. (**A**) Optimal structure of water/CeO_2(111) interface. (**B**) Summary of calculated NMR chemical shifts. The chemical shifts of oxygen ions in the 1st, 2nd and 3rd surface layers, hydroxyl groups are in green, violet, yellow and blue, respectively. Each oxygen ion is labelled and the corresponding NMR parameters for quadrupolar interaction (C_Q, η_Q and ν_Q) and chemical shift are shown in Table S4 and Table S5, respectively.

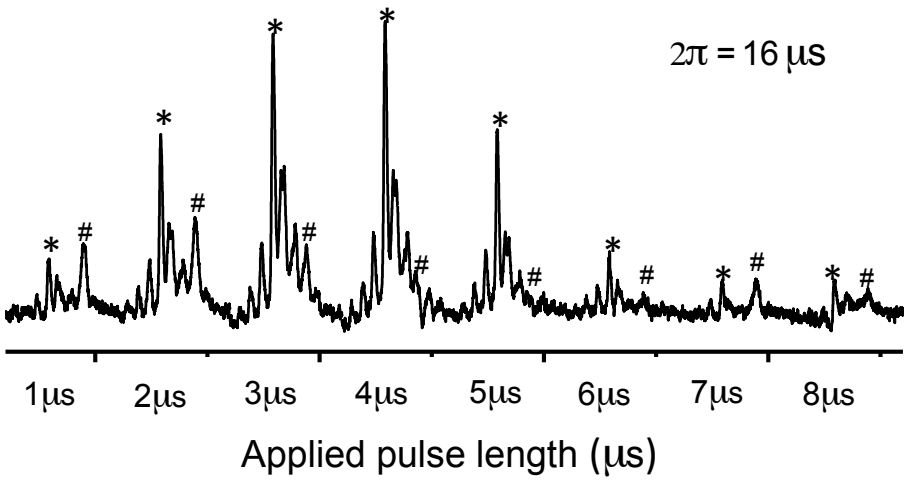

Fig. S9. Nutation NMR of ceria nanoparticles. ^{17}O NMR nutation curves for the peaks at 1040 ppm (∗) and 270 ppm (#) measured on the ceria nanoparticles enriched in $^{17}O_2$ at 573 K. Spectra are plotted as a function of the pulse length. The pulse length was incremented in steps of 1.0 μs from 1.0 to 8.0 μs corresponding to about π/8 to π for water. Field, 9.4 T; spinning speed, 14 kHz; recycle delay, 0.2 s; number of scans, 10,000.

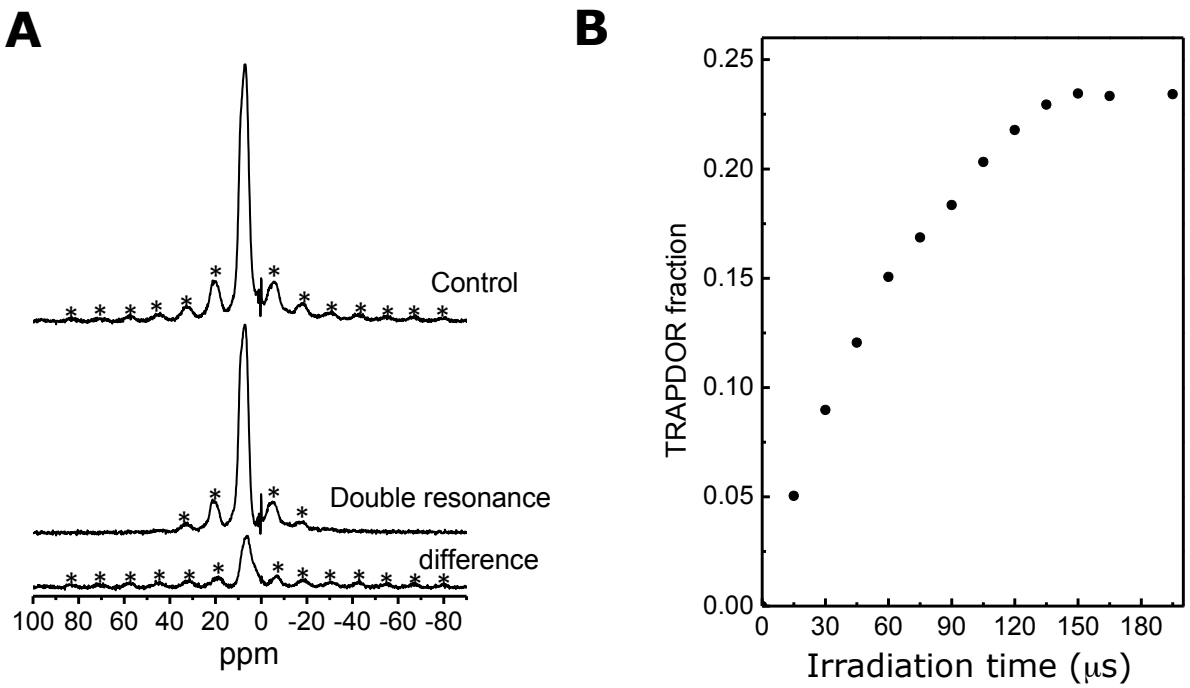

Fig. S10. TRAPDOR NMR of ceria nanoparticles. (**A**) ^{1}H-^{17}O TRAPDOR NMR spectra at an irradiation time of 120 μs (and a ^{17}O radio-frequency field strength of 62.5 kHz determined with $H_2{}^{17}O$) of nanosized ceria enriched with ^{17}O-water (the non-enriched ceria nanoparticles were adsorbed with ^{17}O-water over the vacuum line before it was dried under vacuum at 373 K). Field, 9.4 T; spinning speed, 5 kHz; recycle delay, 4 s. (**B**) Plot of the ^{1}H-^{17}O TRAPDOR fractions ΔS/S0 as a function of irradiation time.

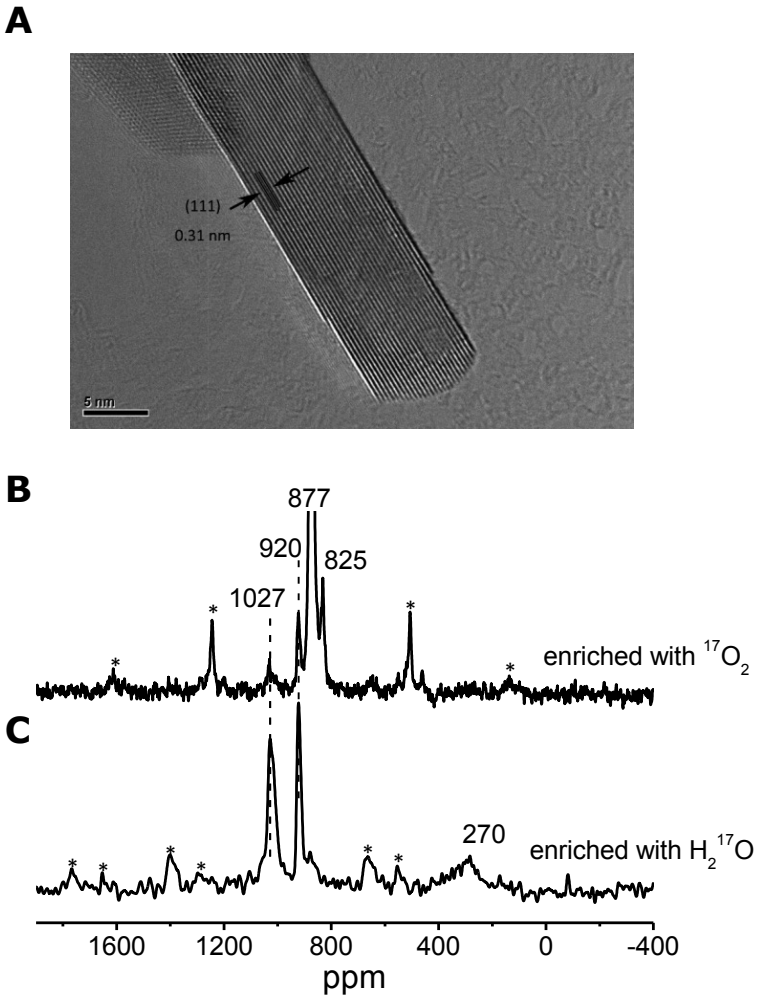

Fig. S11. Electron microscopy and solid-state NMR spectra of ceria nanorods. (**A**) HRTEM image of ceria nanorods with (111) facets exposed. (**B**) ^{17}O MAS NMR spectra of ceria nanorods labelled by heating in $^{17}O_2$ (70 % ^{17}O) at 923 K. (**C**) ^{17}O MAS NMR spectra of ceria nanorods labelled by adsorbing $H_2{}^{17}O$ (70 % ^{17}O) at room temperature followed by thermal treatment at 373 K under vacuum. Field, 9.4 T; spinning speed, 20 kHz. "∗" denotes spinning sidebands.

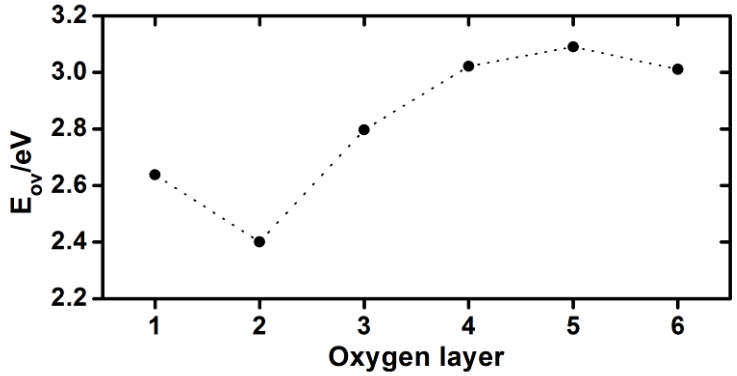

Fig. S12. Vacancy formation energies of different oxygen ions. Vacancy formation energies of oxygen ions at different surface layers in a structural model shown in Fig. 1B.

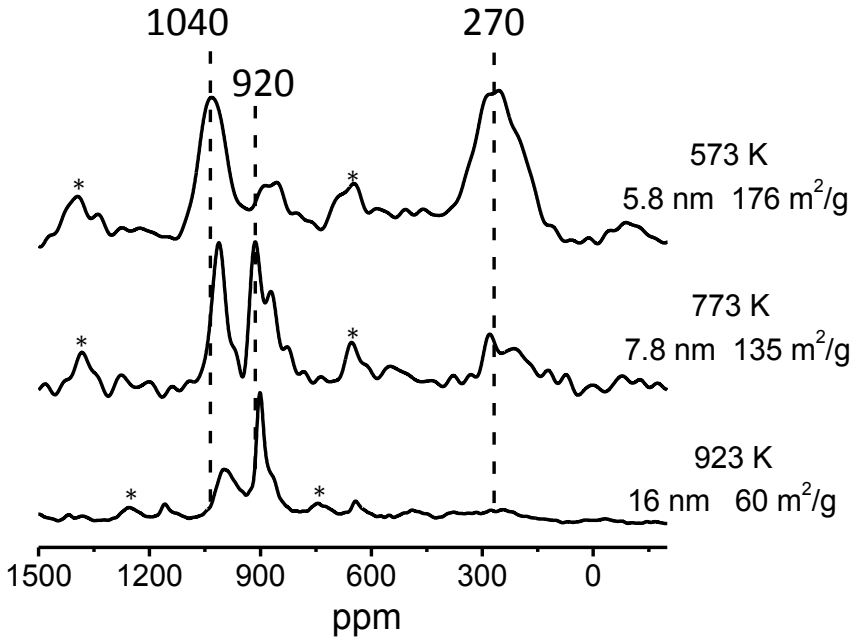

Fig. S13. Solid-state NMR spectra of ceria nanoparticles with different surface area labelled by adsorbing $H_2{}^{17}O$. ^{17}O MAS NMR spectra of nanosized ceria samples pre-heated at different temperature followed by ^{17}O enrichment with $H_2{}^{17}O$ (70 % ^{17}O) (the non-enriched samples were adsorbed with ^{17}O-water over the vacuum line before it was dried under vacuum at 373 K). Short pulse lengths of $\pi/6$ and recycle delays of 0.1 s were used. Field, 9.4 T; spinning speed, 20 kHz (573 K, 773 K) or 14 kHz (923 K); number of scans, 20,000 (573 K, 773 K) and 200,000 (923 K). "$*$" denotes spinning sidebands.

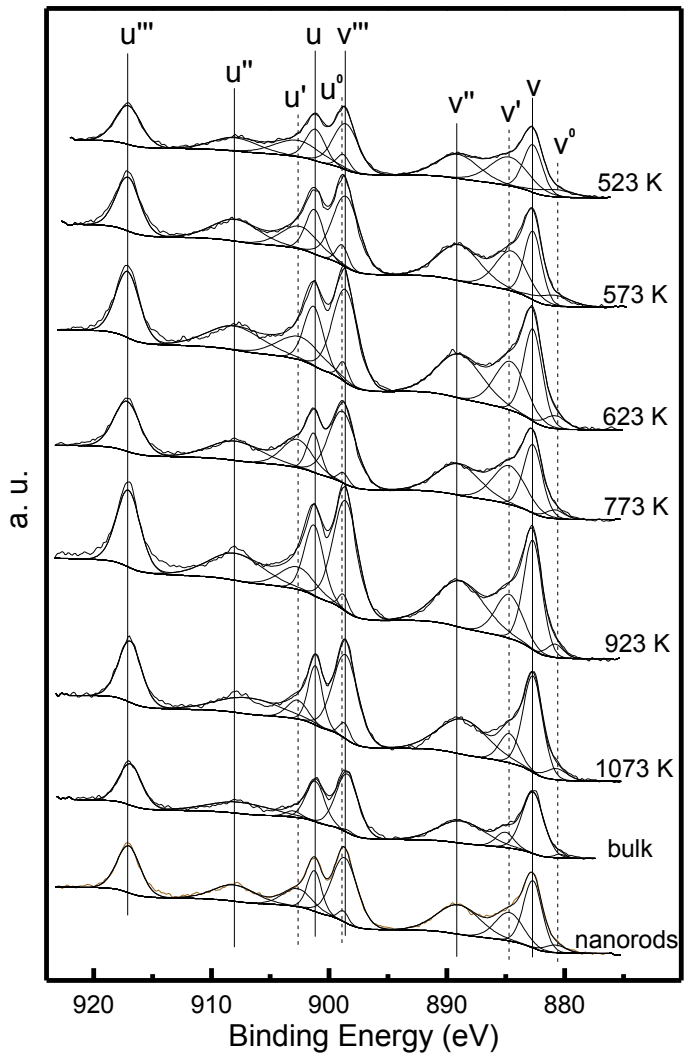

Fig. S14. Ce $3d_{3/2,5/2}$ XPS spectra collected for ceria nanoparticles, nanorods and bulk sample, as well as line fitting results. v^0, v', u^0 and u' peaks are attributed to Ce^{3+}; while v, v'', v''', u, u'', and u''' are the characteristic peaks of Ce^{4+} ions. For Ce^{3+}, the binding energy peaks v^0 and u^0 at 880.6 and 898.8 eV, respectively, correspond to the Ce $3d^9 4f^2$ O $2p^5$ final state; the binding energy peaks v' and u' at about 884.7 and 902.7 eV, respectively, can be attributed to the Ce $3d^9 4f^1$ O $2p^6$ final state. For Ce^{4+}, the binding energy peaks v, u and v'', u'' at 882.7, 901.2, 888.9 and 907.7 eV, respectively, arise from Ce $3d9^4f^2$ O $2p^4$ and Ce $3d^9 4f^1$ O $2p^5$ final states; the binding energy peaks, v''' and u''' at about 898.6 and 917.0 eV, respectively, are due to the Ce $3d^9 4f^0$ O $2p^6$ final state.[27, 28]

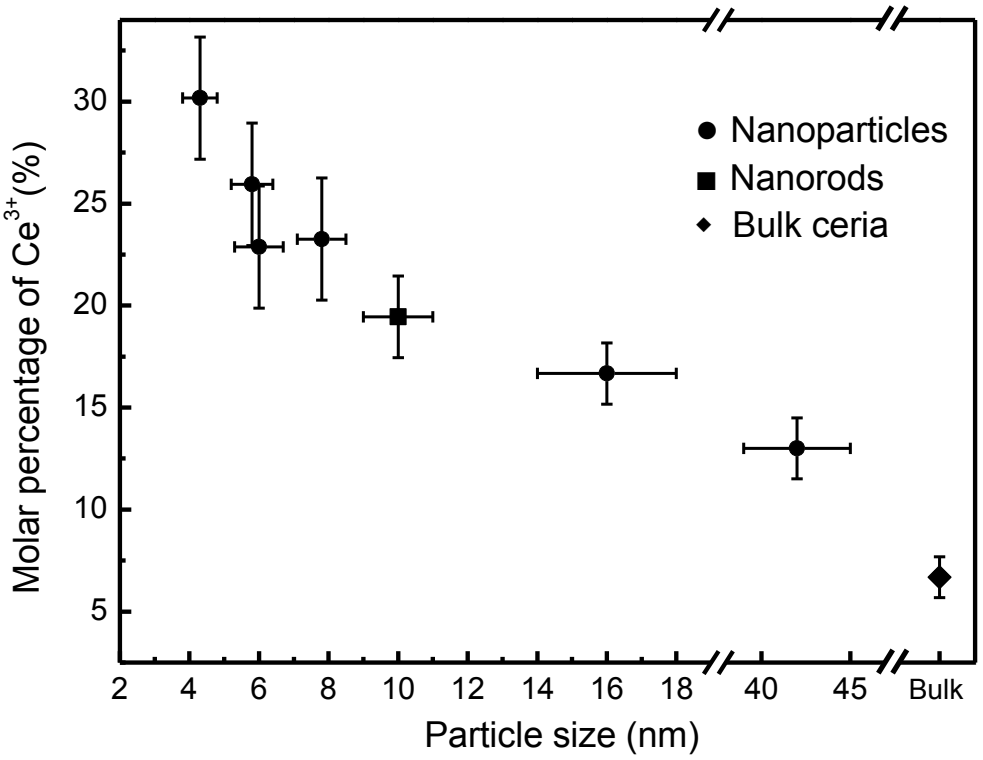

Fig. S15. The molar percentage of Ce^{3+} as a function of particle size from XPS data. The molar percentage of Ce^{3+} is calculated by using [27, 28]

$$[Ce^{3+}] = \frac{A_{v^o} + A_{v'} + A_{u^o} + A_{u'}}{A_{v^o} + A_{v} + A_{v'} + A_{v''} + A_{v'''} + A_{u^o} + A_{u} + A_{u'} + A_{u''} + A_{u'''}},$$

where A_i is the integrated area of peak "i." in the XPS data shown in Fig. S14

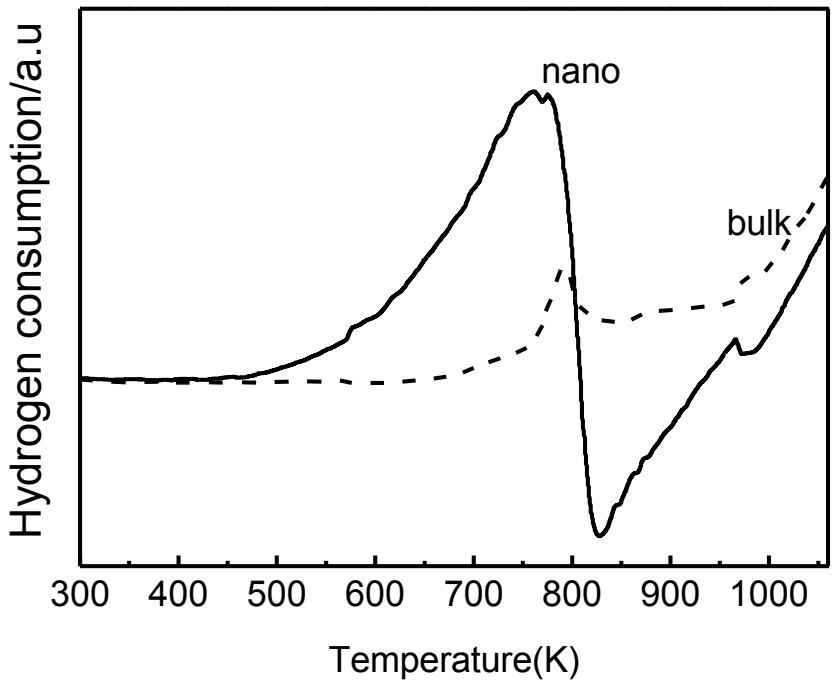

Fig. S16. H_2 temperature programmed reduction (TPR) profiles of bulk ceria and ceria nanoparticles.

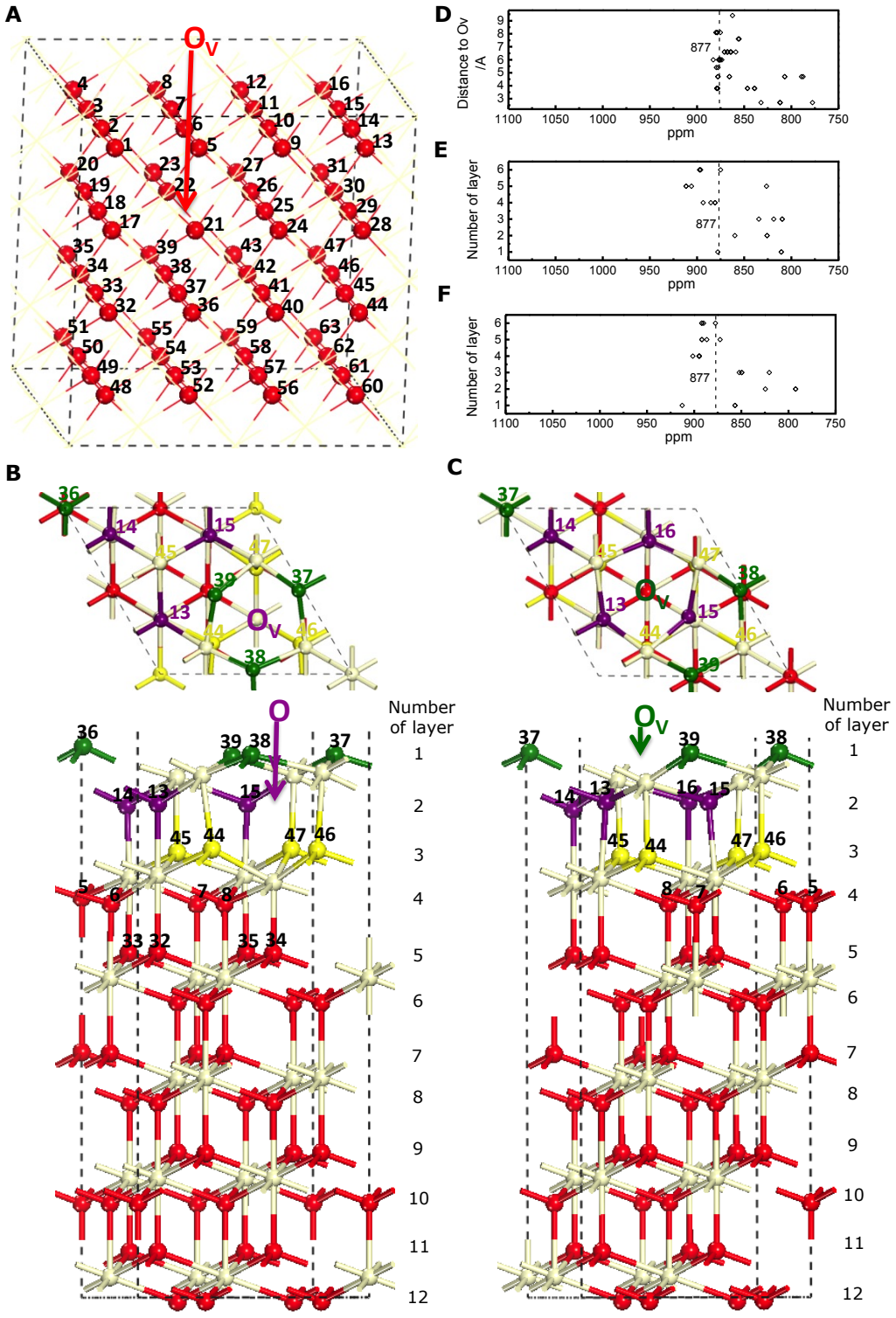

Fig. S17. The structure model and chemical shift calculations of ceria with oxygen vacancies. The structural model of ceria for DFT calculations of the effects of an oxygen vacancy on the NMR chemical shift. Calculated structures of (**A**) CeO_2 (2×2×2) unit cell with an oxygen vacancy, (**B**) CeO_2(111) with a sub-surface oxygen vacancy (top and side views) and (**C**)

CeO_2(111) with a surface oxygen vacancy (top and side views). (**D**, **E**, **F**) Summary of the corresponding calculated NMR chemical shifts (See Table S6-8 for details). Oxygen ions in the 1^{st}, 2^{nd} and 3^{rd} surface layers of (b, c) are in green, violet and yellow, respectively. Each oxygen ion close to the vacancy is labelled and the corresponding chemical shift is shown in Table S6-8.

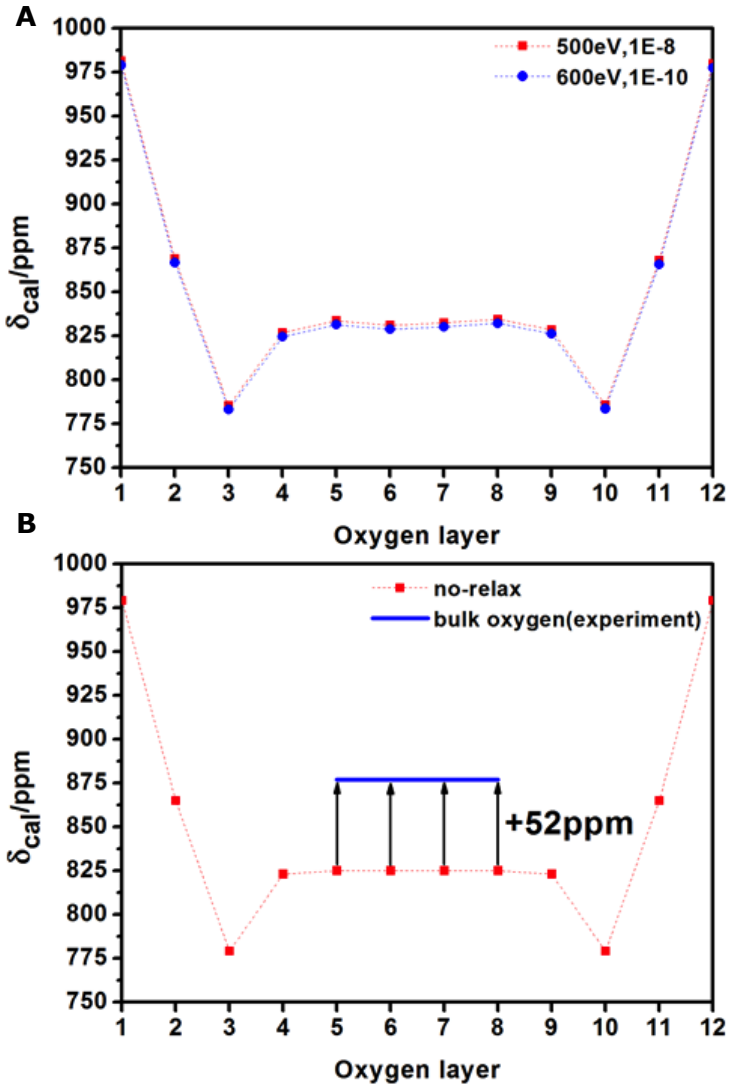

Fig. S18. The criterion for NMR calculations and the determination of chemical shift. (**A**) Test on the cutoff and stopping-criterion for electronic minimization at clean CeO_2(111). (**B**) Determination of the reference chemical shift (δ_{ref}).

Table S1. Mean diameter of ceria nanoparticles. Mean diameter (D_{XRD}) of ceria nanoparticles calcined at different temperatures in a $^{17}O_2$ atmosphere calculated based on the XRD data (Fig. S2) by using the Debye-Scherrer equation.

Temperature (K)	D_{XRD} (nm)
523	4.3 (5)
573	5.8 (6)
623	6.0 (7)
773	7.8 (7)
923	16.0 (20)
1073	42.0 (30)

Table S2. BET surface area of ceria samples. BET surface area of ceria nanoparticles calcined at different temperature in comparison with bulk ceria.

Temperature (K)	BET Surface Area ($m^2 \cdot g^{-1}$)
523	190
573	176
623	166
773	135
923	60
1073	25
Bulk	6

Table S3. Calculated NMR parameters of quadrupolar interaction for ceria. Calculated C_Q, η_Q and ν_Q of oxygen ions in the structural model shown in Fig. 1B.

Layer	C_Q (kHz)	ν_Q (kHz)	η
1	135	20.3	0.004
2	107	16.1	0.002
3	117	17.6	0.009
4	23	3.5	0.029
5	26	3.9	0.019
6	23	3.5	0.067
7	10	1.5	0.168
8	10	1.5	0.128
9	5	0.8	0.235
10	123	18.5	0.019
11	99	14.9	0.012
12	144	21.6	0.001

Table S4. Calculated NMR parameters of quadrupolar interaction for ceria in contact with water. Calculated C_Q, η_Q and ν_Q of oxygen ions in the structural model shown in Fig. S8A. The number in the parenthesis corresponds to the labelling of the oxygen ion shown in Fig. S8A.

Number	Layer	C_Q (kHz)	ν_Q (kHz)	η
1	3	117	17.6	0.115
2		117	17.6	0.757
3		122	18.3	0.916
4		92	13.8	0.146
5	4	46	6.9	0.641
6		49	7.4	0.684
7		107	16.1	0.217
8		130	19.5	0.069
9	5	53	8.0	0.061
10		46	6.9	0.141
11		64	9.6	0.128
12		61	9.2	0.109
13	2	221	33.2	0.827
14		167	25.1	0.769
15		193	29.0	0.566
16		223	33.5	0.409
17	1	563	84.5	0.876

18		373	56.0	0.926
19(OH group)		5019	752.9	0.073
20		396	59.4	0.259
21		24	3.6	0.785
22		24	3.6	0.732
23	6	57	8.6	0.313
24		24	3.6	0.038
25		357	53.6	0.545
26		277	41.6	0.594
27	2	243	36.5	0.391
28		305	45.8	0.523
29		12	1.8	0.895
30		12	1.8	0.960
31	6	13	2.0	0.439
32		8	1.2	0.645
33		51	7.7	0.926
34		72	10.8	0.386
35	5	48	7.2	0.917
36		48	7.2	0.925
37		594	89.1	0.200
38		511	76.7	0.417
39	1	170	25.5	0.909
40		214	32.1	0.182

41	4	51	7.7	0.497
42		36	5.4	0.871
43		57	8.6	0.788
44		48	7.2	0.674
45	3	94	14.1	0.706
46		133	20.0	0.697
47		62	9.3	0.743
48		114	17.1	0.694

Table S5. Calculated chemical shifts for ceria in contact with water. Calculated chemical shifts for oxygen ions in the structure of water/CeO_2(111) shown in Fig. S8A. The number in the parenthesis under the chemical shift corresponds to the labelling of the oxygen ion shown in Fig. S8A.

Number of Layer	δ_{iso} / ppm							
1(OH)	(P_Q=5.0 MHz)			366 (19)				
1	1068.1 (17)	1076.1 (18)	935.0 (20)		1048.8 (37)	890.9 (38)	919.7 (39)	937.9 (40)
2	920.7 (25)	861.1 (26)	940.0 (27)	940.0 (28)	917.1 (13)	923.1 (14)	928.4 (15)	911.5 (16)
3	819.5 (1)	850.7 (2)	896.2 (3)	882.5 (4)	855.1 (45)	863.0 (46)	880.0 (47)	823.9 (48)
4	886.0 (41)	884.1 (42)	887.1 (43)	889.1 (44)	883.9 (5)	884.2 (6)	890.3 (7)	878.0 (8)
5	892.7 (9)	890.8 (10)	884.5 (11)	888.3 (12)	887.7 (33)	883.4 (34)	896.4 (35)	895.4 (36)
6	888.7 (29)	888.7 (30)	889.3 (31)	886.4 (32)	889.3 (21)	889.2 (22)	882.7 (23)	888.0 (24)

Table S6. Calculated chemical shifts for ceria with oxygen vacancies in the bulk. Calculated chemical shifts for oxygen ions close to an oxygen vacancy in CeO_2 (2×2×2) unit cell (a=5.448 Å) with an oxygen vacancy (O_V) described in Fig. S17A. The number in the parenthesis under the chemical shift corresponds to the labelling of the oxygen ion shown in Fig. S17A.

Coordination Shell	Distance to O_V /Å	δ_{iso} / ppm								Average / ppm
Nearest	2.7	812.2	811.7	811.7	812.2	832.2	777.6			
	(a/2)	(22)	(18)	(21)	(25)	(6)	(37)			
		878.1	846.4	878.1	846.6	879.0	878.9	879.0	878.9	
Second	3.8	(19)	(17)	(24)	(26)	(7)	(2)	(5)	(10)	840.6
	(a/2×√2)	839.0	839.1	839.1	839.0					
		(38)	(33)	(36)	(41)					
Third	4.7	877.6	807.1	807.1	878.1	865.7	787.6	865.7	789.3	
	(a/2×√3)	(1)	(3)	(9)	(10)	(34)	(32)	(40)	(42)	
		877.7	877.7	879.6	875.6	875.3	875.3	875.6	875.3	
		877.0	876.5	876.5	877.0	873.7	873.7	882.8	882.8	
	≥5.4	878.8	855.3	878.6	862.5	878.6	855.3	878.8	880.0	872.0
		876.5	867.7	867.9	867.9	867.7	864.4	863.9	863.9	
		864.4	870.9	858.9	858.9	870.9				

Table S7. Calculated chemical shifts for ceria with sub-surface oxygen vacancies. Calculated chemical shifts for oxygen ions close to an oxygen vacancy in $CeO_2(111)$ with a sub-surface oxygen vacancy described in Fig. S17B. The number in the parenthesis under the chemical shift corresponds to the labelling of the oxygen ion shown in Fig. S17B.

Number of Layer	δ_{iso} / ppm				Average δ_{iso} /ppm
1	727.6 (36)	810.6 (37)	810.6 (38)	878.0 (39)	
2	825.7 (13)	859.8 (14)	825.7 (15)		
3	809.7 (44)	834.4 (45)	818.7 (46)	809.7 (47)	847.7
4	885.4 (5)	880.9 (6)	880.9 (7)	893.5 (8)	
5	911.7 (32)	906.0 (33)	826.3 (34)	911.7 (35)	

Table S8. Calculated chemical shifts for ceria with surface oxygen vacancies. Calculated chemical shifts for oxygen ions close to an oxygen vacancy in $CeO_2(111)$ with a surface oxygen vacancy in Fig. S17C. The number in the parenthesis under the chemical shift corresponds to the labelling of the oxygen ion shown in Fig. S17C.

Number of Layer	δ_{iso} / ppm				Average δ_{iso} / ppm
1	912.7 (37)	856.7 (38)	856.6 (39)		846.0
2	792.5 (13)	697.2 (14)	824.5 (15)	792.5 (16)	
3	849.5 (44)	852.1 (45)	820.3 (46)	849.5 (47)	
4	901.4 (5)	894.5 (6)	894.5 (7)	895.0 (8)	

Table S9. Detailed NMR parameters for acquiring ^{17}O MAS NMR data in Fig. 1.

Enrichment temperature (K)	External field (T)	Probe (mm)	Spinning speed (kHz)	Pulse width (μs)	Recycle delay (s)	Number of acquisitions	Data collection time (h)
573	14.1	1.3	55	0.3 (π/18)	2	4096	2.3
523	9.4	3.2	20	0.4 (π/18)	1	50000	13.9
573	9.4	3.2	20	0.4 (π/18)	2	1024	0.6
623	9.4	3.2	20	0.4 (π/18)	2	1024	0.6
773	9.4	3.2	20	0.4 (π/18)	8	1024	2.3
923	9.4	3.2	20	0.1 (π/72)	4	1024	1.1
1073	9.4	3.2	20	0.1 (π/72)	100	16	0.4
1073 (bulk)	9.4	3.2	20	0.1 (π/72)	100	16	0.4

Table S10. Detailed NMR parameters for acquiring ^{17}O NMR data in Fig. 2.

Experiment Label	Recycle delay (s)	Number of acquisitions	Data collection time (h)
Fig. 2A-nano ceria*	1	4096	1.1
Fig. 2A-nano-H_2O dried at 573 K	1	4096	1.1
Fig. 2A-nano-H_2O dried at RT	1	4096	1.1
Fig. 2A-nano-H_2O	0.2	8192	0.5
Fig. 2A-nano ceria exposed in air	0.2	8192	0.5
Fig. 2A-nano-H_2O (natural)	0.2	8192	0.5
Fig. 2B-nano-$H_2{}^{17}O$(A)	0.1	40000	1.1
Fig. 2B-nano-$H_2{}^{17}O$(D) dried at 373 K	0.1	8192	0.2
Fig. 2B-nano-$H_2{}^{17}O$(D)	0.1	8192	0.2
Fig. 2B-bulk-$H_2{}^{17}O$ dried at 373 K	0.1	8192	0.2
Fig. 2B-bulk-$H_2{}^{17}O$	0.1	8192	0.2
Fig. 2B-$H_2{}^{17}O$	0.1	64	0.002

* The liquid water (Fig. 2B-$H_2{}^{17}O$) was measured in a static experiment with one pulse sequence. In all the other experiments, a rotor synchronized Hahn-echo sequence ($\pi/6 - \tau - \pi/3 - \tau$ - acquisition) was used under a MAS rate of 20 kHz.